Research Article

Effect of Microstructural Features and Al₂O₃ Doping on Aging Resistance, Mechanical Properties and Crack Propagation in 3Y-TZP Plate Ceramics for Dental Restorations: A Comprehensive Peridynamics Study

Alireza Moradkhani [ID], Mohammad Hoseinpour *[ID], Valiollah Panahizadeh [ID]

Department of Mechanical Engineering, Shahid Rajaee Teacher Training University, Tehran, Iran

ARTICLE INFO

ABSTRACT

This study investigates the effects of microstructural features, nanoporosity, and micro-cracks on macro-crack propagation in 3Y-TZP plate ceramics doped with Al₂O₃ (0 to 0.5 wt%) for dental restoration applications, utilizing peridynamics (PD) theory for the first time. The research employs ordinary state-based PD to offer new insights into these interactions. Materials are synthesized through high-energy ball milling of ZrO₂ powders at 1500 °C for 2 h. Mechanical properties, including density, average porosity diameter, Young's modulus, Poisson's ratio, and fracture toughness (K_{IC}), are rigorously assessed. Results indicate that increasing Al₂O₃ content to 0.05 wt% enhances relative density, hardness, Young's modulus, K_{IC}, and flexural strength to 99.5%, 15.1 GPa, 280 GPa, 9.97 MPa·m$^{1/2}$, and 355 MPa, respectively, while low-temperature degradation over 800 h shows that Al₂O₃ doping significantly reduces aging kinetics. PD simulations demonstrate that micro-cracks substantially affect crack propagation, revealing a 15% reduction in macro-crack speeds compared to FEM results. This research enhances the understanding of dental ceramics and establishes a foundation for analyzing fractures in dental restoration ceramics using PD.

1. Introduction

Zirconia (ZrO₂) is a polycrystalline metal oxide ceramic known for its unique physical, chemical, mechanical, and clinical properties, making it suitable for hard biological tissues and dental restorations [1-2]. It is non-toxic and exhibits excellent bio-compatibility [3]. ZrO₂'s high strength and fracture toughness (K_{IC}) enhance its desirability in dentistry, where it closely mimics the natural appearance of teeth [4].

To mitigate phase transformations that can cause micro-cracks, metal oxides like CaO [5], MgO [6], CeO₂ [7], Er₂O₃ [8], and Y₂O₃ [9] are added to pure ZrO₂, resulting in partially stabilized zirconia (PSZ) that remains stable at room temperature [10]. PSZ can exist in cubic (c), tetragonal (t), and monoclinic (m) phases, with yttria (Y₂O₃) often used to favor the tetragonal

* Corresponding author.
E-mail address: m.hoseinpour@sru.ac.ir

phase [11]. Among these, 3 mol% yttria-tetragonal zirconia (3Y-TZP) is the most commonly used in dental restorations, including crowns, inlays, onlays, abutments, and implants [12]. Figure 1 illustrates some applications of 3Y-TZP in dental restoration.

Research has shown interest in doping 3Y-TZP with rare earth oxides. Zhang *et* al. [13] found that alumina (Al_2O_3) co-doping enhances translucency and mechanical properties. Samodurova *et* al. [14] reported improvements in mechanical properties with Al_2O_3 and silica co-doping. Seesala *et* al. [15] demonstrated that Al_2O_3 coatings on zirconia implants improve strength and aging resistance. Salma [16] explored microstructure development in YSZ-

added Al_2O_3 composites to optimize fracture toughness and stress resistance.

Figure 2 shows three ZrO_2 crystal structures that can transform with changes in density, depending on the temperature range. Maintaining ZrO_2 in a tetragonal phase at room temperature enhances its mechanical and aesthetic properties. Under stress, the material undergoes martensitic transformation, which helps absorb stress and improve crack resistance through transformation toughening. However, the K_{IC} of 3Y-TZP is moderate (4-5 $MPam^{1/2}$), and it is susceptible to low-temperature degradation (LTD) [17, 18].

Fig. 1. Applications of 3Y-TZP in dental restorations (a) Full crown; (b) Inlay and Onlay (c) Abutment and Implant
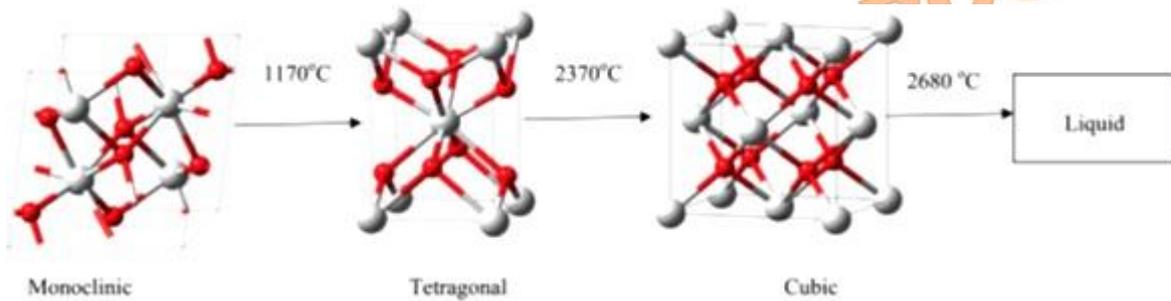

Fig. 2. Crystal structure of three monoclinic, tetragonal, and cubic phases and their transformation temperature

Rietveld analysis is a powerful and widely used technique in the field of crystallography. It is a method for refining crystal structures from X-ray or neutron diffraction data. Rietveld analysis allows researchers to determine the precise atomic arrangement within a crystal lattice by comparing experimental diffraction patterns with theoretical patterns calculated from a structural model [19].

The issue of failure in brittle materials has always been pertinent in engineering practice. One prevalent form of mechanical failure is known as brittle fracture [20, 21]. The weakening and abrupt collapse of the structure can occur as a result of mechanical failure, occlusal loading, and imperfections in dental materials. [22]. Restorative brittle materials used in dental treatments can contain small-sized defects such as micro-cracks and micro-porosities, which are randomly dispersed [23, 24]. The presence of these defects can greatly impact the way macro-cracks propagate. The interaction between macro and micro-cracks has been a focus of several

experimental investigations in the literature [25, 26]. Various studies indicate that the presence of micro-cracks can result in a phenomenon known as "micro-crack toughening" [27]. Micro-cracks can serve as inhibitors of crack propagation and play a role in expanding the fracture zone [28, 29]. Moreover, the stress shielding effects resulting from the interaction between micro and macro cracks can depend on factors such as their distribution, distances, sizes, and inclination angles. This interaction can cause a decrease in the stress intensity factor (SIF) [30].

Numerous analytical studies have been conducted to explore various scenarios, such as the presence of a micro-crack positioned ahead of the primary crack [31], the primary crack's interaction and various arrays of micro-cracks [32], and the distribution of micro-cracks surrounding the main crack [33]. These studies entail examining the stress fields near the crack tip, which are defined by parameters such as K_0S for models featuring a macro-crack and K_lSIF for diverse configurations of micro-cracks. The

2

interaction between the macro-crack and micro-cracks is quantified utilizing the K_I/K_0, which helps determine whether micro-cracks promote or hinder the propagation of the macro-crack and offers insights into the complex structural response in the presence of defects. Moreover, when a plate contains both macro-cracks and micro-cracks, the presence of micro-cracks can influence the behavior of the primary crack [34, 35]. In certain cases, the primary crack may align with the orientation of the micro-cracks, indicating the impact of micro-cracks on the propagation characteristics of the main crack. Traditional continuum mechanics-based methods have been utilized to tackle the intricate issues related to crack interactions. However, these methods often involve simplifications and assumptions to facilitate problem-solving. For instance, mathematical computations frequently concentrate on the relationship between the primary crack and micro-cracks, disregarding the possible mutual interactions among the micro-cracks themselves [27, 34].

Some studies focusing on the interaction between cracks and holes such as porosities have revealed the occurrence of momentary crack arrest phenomena [36].

These investigations have demonstrated that in dental restoration materials with micro-porosity defects, crack propagation can be momentarily interrupted before resuming with increased speed. The location and size of the defects, as well as the loading rates, determine whether the crack can be stopped or continue through the porosities. When a micro-porosity is positioned off-center from the main crack, the crack deflects towards it before returning to its original path [37]. This behavior suggests that the presence of micro-porosity can affect the path of crack propagation. Milios and Spathis [38] examined how the imbalance of the stress field near a micro-hole can lead to the curvature of a propagating crack, resulting in crack arrest. Additionally, the variation in the K_I/K_0 was explored in [39], highlighting that the SIF values increase during the crack arrest phase. This indicates that changes in SIF values influence the halting of crack propagation. An integral equation method was suggested to investigate the configurations of voids, including holes, porosities, and cracks [40]. These studies showed that the presence of porosities may result in toughening effects within the material structure. This underscores the importance of considering the sizes and distribution of porosities, as they significantly impact stress mitigation or amplification. Therefore, meticulous attention to micro-porosity sizes and their spatial distribution is essential for understanding the overall performance and durability of dental

ceramics. The topic of structural defects has been a focal point in the literature. Although experimental fracture analyses are beneficial, they can be expensive and demand meticulous control to guarantee precision.

Numerical tools provide a valuable alternative for investigating fracture behavior and mechanisms, offering a way to overcome the limitations and expenses associated with experimental testing. The finite element method (FEM) has been utilized for predicting brittle fracture, simulating crack propagation, and modeling crack branching. FEM is based on classical continuum mechanics equations expressed as partial differential equations. To simulate crack propagation accurately, Tracking the crack surface, determining crack growth direction, and assessing the SIF are crucial for understanding crack propagation and material failure [41]. In addition, FEM is mesh-dependent, necessitating model re-meshing after each propagation step to address crack growth challenges. To overcome these issues, the extended finite element method (XFEM) was developed to handle problems involving discontinuities like cracks [42]. In XFEM, cracks are modeled independently of the mesh, leading to more precise simulations. XFEM has proven effective in various scenarios involving interactions between macro- and micro-cracks [43]. However, determining the shape and position of the crack tip remains a critical aspect that requires careful consideration.

As an alternative to classical continuum mechanics, Silling [44] introduced a novel numerical approach for fracture analysis known as peridynamics (PD). PD models employ integro-differential equations rather than partial differential equations, enabling the examination of intricate crack interaction scenarios without the necessity of tracking crack tip positions or behavior. The original "bond-based" PD formulation has proven to be effective in addressing brittle fracture issues by accurately forecasting crack initiation, propagation [45-48], and the interaction between primary cracks and micro-cracks [49, 50]. The commonly used "bond-based" PD model has limitations in defining material properties, as it enforces Poisson's ratio to 1/3 in 2D models and 1/4 in 3D models [51]. To address this constraint, Silling et al. [52] introduced the ordinary state-based PD method. This enhanced model allows for varying Poisson's ratios in 2D and 3D models, offering more realistic outcomes compared to the restricted 1/3 and 1/4 ratios [26].

This study presents a comprehensive examination of PD in dental restorations for the first time. It investigates the effects of nanoporosity and micro-cracks on the

propagation of macro-cracks in 3Y-TZP ceramics with low Al_2O_3 content, an area that has not been extensively explored by researchers. The research integrates experimental data with results from PD and FEM theories to assess how these factors affect crack propagation behavior in dental ceramics. Various 3Y-TZP dental ceramics were synthesized with Al_2O_3 doping levels of 0, 0.02, 0.05, 0.1, 0.2, 0.25, 0.3, and 0.5 wt% through high-energy ball milling of ZrO_2 powders. The mechanical properties and LTD of the dental plate samples were evaluated. A brief introduction to ordinary state-based PD is provided, and PD simulations are employed to explore the influence of nanoporosities and micro-cracks on macro-crack propagation. The critical loads for five different scenarios involving micro-crack presence are compared with analytical solutions.

2. PD Formulation in Dental Plate Ceramics

The state-based peridynamic method, introduced by Silling and Askari [53], presents a redefined set of equations from continuum mechanics that is particularly adept at handling issues related to discontinuities. PD utilizes integro-differential equations, a departure from the partial differential equations used in classical continuum mechanics. This expanded framework allows for the resolution of fracture mechanics challenges, including the onset and advancement of cracks. The equation of motion in PD can be represented as an integrodifferential equation, as in equation 1, offering a unique approach to modeling material behavior [54]:

$$\rho \ddot{u}(x,t) = \int_H \left(t\left(u'-u, x'-x, t\right) - t\left(u-u', x-x', t\right) \right) dV' + b(x,t) \tag{1}$$

where H is a neighborhood of x, u is the displacement vector field, b is a prescribed body force density field, ρ is mass density in the reference configuration, and t is a pairwise force function whose value is the force vector that the particle x' exerts on the particle x. The above equation can be discretized as shown in equation 2 [26]:

$$\rho_{(i)} \ddot{u}_{(i)} = \sum_{j=1}^{N} \left(t_{(i)(j)} \left(u_j - u_i, x_{(j)} - x_{(i)}, t \right) - t_{(j)(i)} \left(u_{(i)} - u_{(j)}, x_{(i)} - x_{(j)}, t \right) \right) V_{(j)} + b_{(i)} \tag{2}$$

The acceleration of material point i at time t, denoted as $\ddot{u}_{(i)}$, can be obtained through discretization in dental ceramics. Material point i interacts with other points j within its horizon $H_{x(i)}$, with a total of N family members for point i. This interaction is shown in Figure 3.
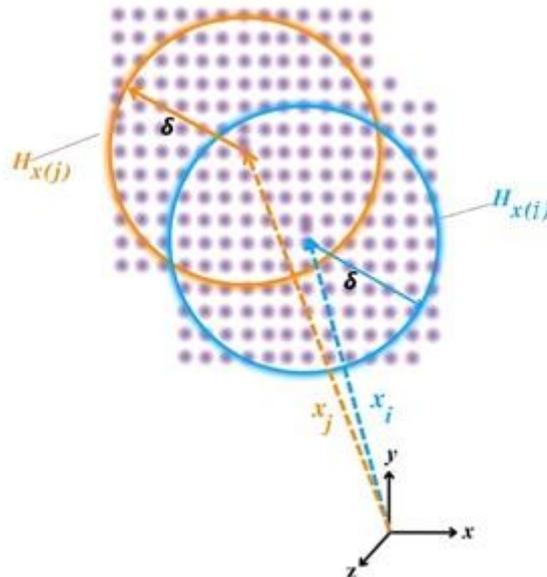

Fig. 3. Peridynamic material points and their interaction within the dental plate

The material point's position is marked by x in a volume V. The displacement field, body load, and mass density are denoted as u, b, and ρ. In dental ceramic plate simulations, the horizontal and vertical displacements are represented by u and v. In a 2-D context, the interaction between

4

material points i and j can result in unequal forces in the ordinary state-based PD method [55]. The PD force densities for points i and j are outlined in equations 3 and 4 [26]:

$$t_{(i)(j)} = 2\delta \left(d \frac{\Lambda_{(i)(j)}}{\left| x_{(j)} - x_{(i)} \right|} a\theta_{(i)} + 2\delta b s_{(i)(j)} \right) \times \frac{y_{(j)} - y_{(i)}}{\left| y_{(j)} - y_{(i)} \right|} \tag{3}$$

$$t_{(j)(i)} = -2\delta \left(d \frac{\Lambda_{(i)(j)}}{\left| x_{(j)} - x_{(i)} \right|} a\theta_{(j)} + 2\delta b s_{(i)(j)} \right) \times \frac{y_{(j)} - y_{(i)}}{\left| y_{(j)} - y_{(i)} \right|} \tag{4}$$

Here, δ is the horizon size, and the parameters a, b, and d are unique to the PD method. The distance between material points is shown as s, and the dilatation, denoted as θ, can be expressed as equation 5 [26]:

$$\theta_{(i)} = d\delta \sum_{j=1}^{N} \Lambda_{(i)(j)} s_{(i)(j)} V_{(j)} \tag{5}$$

$\Lambda_{(i)(j)}$ is defined in equation 6 [26]:

$$\Lambda_{(i)(j)} = \left(\frac{y_{(j)} - y_{(i)}}{\left| y_{(j)} - y_{(i)} \right|} \right) \left(\frac{x_{(j)} - x_{(i)}}{\left| x_{(j)} - x_{(i)} \right|} \right) \tag{6}$$

In the altered state, the updated position of a material point post-deformation is denoted as y, as illustrated in Figure 4.
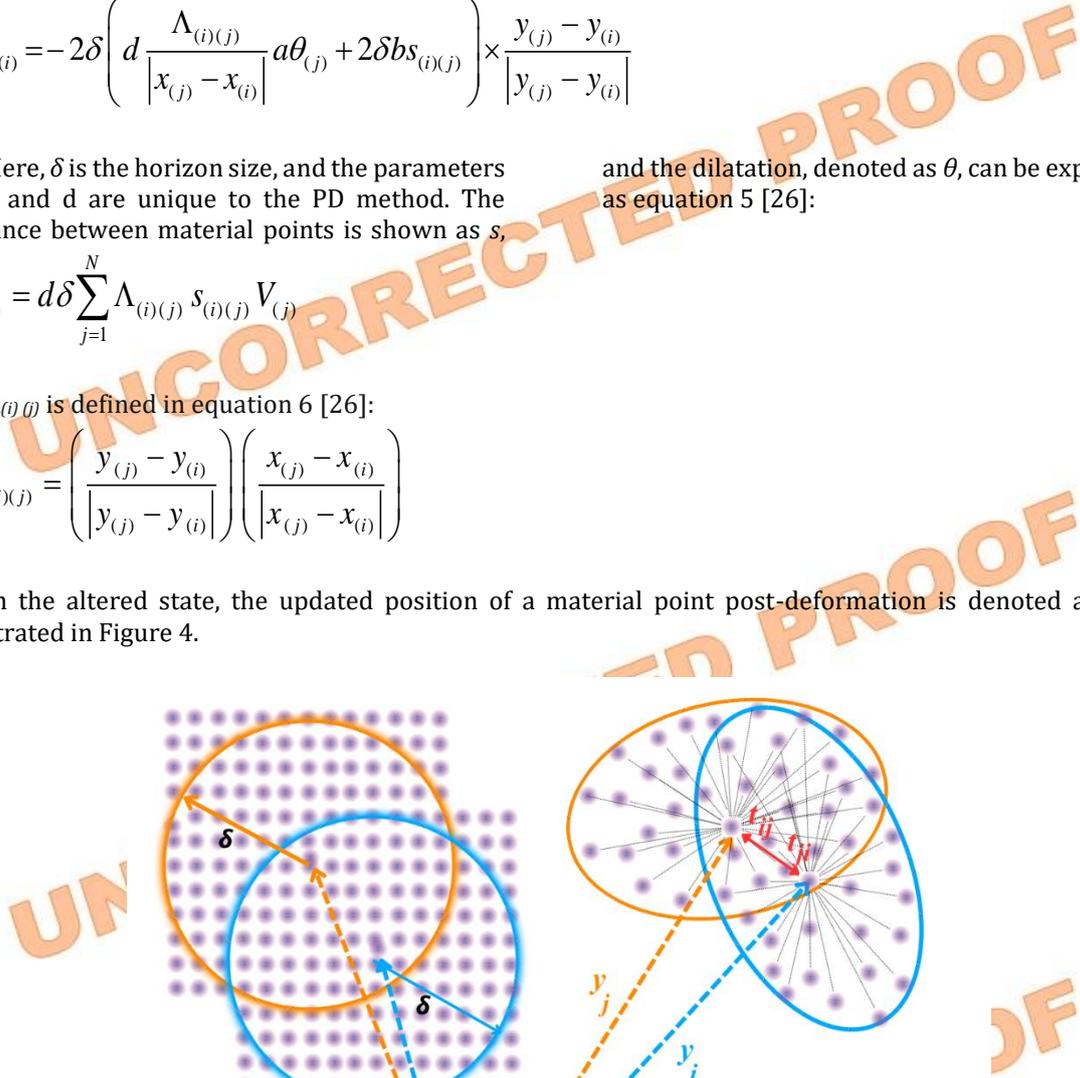

Fig. 4. Peridynamics parameters in undeformed and deformed states

The PD parameters a, b, and d can be determined by equating the strain energy density of a material point inside a body under isotropic expansion and simple shear loading conditions, as calculated using classical continuum mechanics and PD [55]. This allows for a relationship to be established between these PD parameters and the material constants of classical continuum mechanics. This study uses a 2-D model for 3Y-TZP/Al$_2$O$_3$ dental materials in plane stress conditions. The plate is discretized with a single layer in the thickness direction. This allows the expression of the PD parameters as the bulk modulus (κ), thickness (h), shear modulus (μ), and horizon size (δ) for the 2-D problem presented in equation 7 [55]:

5

$$a = \frac{1}{2}(\kappa - 2\mu), b = \frac{6\mu}{\pi h \delta^4}, d = \frac{6\mu}{\pi h \delta^3} \tag{7}$$

This modeling method is important as dental restorative materials such as crowns, inlays, onlays, abutments, and veneers on implants often encounter surface tension during chewing.

$$s_{(i)(j)} = 1 - \frac{\left(|y_j - y_i| - |x_j - x_i| \right)}{|x_j - x_i|} \tag{8}$$

Silling and Bobaru [56] introduced a failure parameter that incorporates a history-dependent scalar-valued function μ. This

$$\mu\left(x_{(j)} - x_{(i)}, t\right) = \begin{cases} 1 & s_{(i)(j)}\left(x_{(j)}, x_{(i)}, t'\right) < s_c \quad 0 < t' \\ 0 & \text{otherwise} \end{cases} \tag{9}$$

In equation 9, S_c denotes the critical stretch, which can be defined for a 2-D scenario in equation 10 [55]:

$$s_c = \sqrt{\frac{G_c}{\left(\frac{6}{\pi}\mu + \frac{16}{9\pi^2}(\kappa - 2\mu)\right)\delta}} \tag{10}$$

In this equation, the critical energy release rate is represented by G_c. The local damage of

Therefore, the tension between dental material points i and j can be described in equation 8 [26]:

function is used to represent broken interactions (bonds) between material points, which can be expressed in Equation 9 [56]:

material point i, ranging from 0 to 1, can be expressed in equation 11 [26]:

$$\varphi(x_i, t) = 1 - \frac{\sum_{i=1}^{N} \mu(x_{(j)} - x_{(i)}, t) V_{(j)}}{\sum_{i=1}^{N} V_{(j)}} \tag{11}$$

3. Materials and Methods

3.1. Samples Preparation

Eight different compositions of dental ceramics were investigated. The ZrO_2 powder used in the experiment was prepared through a solid-state reaction high-energy ball milling method. ZrO_2 (Hang-Zhou Wan-Jing Co., AR Grade, purity ≥99.98 %, 500 ± 100 nm) and Y_2O_3 (Shang-Hai Yue-Kai Co., AR Grade, purity ≥99.98 %) were used as raw materials. The eight materials consisted of 3 mol% yttria-stabilized zirconia with varying amounts including 0, 0.02, 0.05, 0.1, 0.20, 0.25, 0.3, and 0.5 wt% of α-Al_2O_3 (Feng-Fan Chemical Co., Ltd., AR Grade, purity ≥ 99.98%) added to form 3Y-TZP. The precise quantities of each component were calculated based on stoichiometry. The powders were subjected to high-energy ball milling at 3000 r/min for 2 h, followed by 2800 r/min for 2 h, and then dried completely to obtain 3Y-TZP powder. To prepare the 3Y-TZP + x wt% Al_2O_3 powder, the

dried powder was additionally dried at 75 °C for 24 h to eliminate any residual ethanol. The resulting powders were uniaxially pressed under 30 MPa and then cold isostatically pressed to form pellets under 200 MPa. The green pellets were sintered in a pressure-less air environment at 1500 °C for 2 h.

3.2. Relative Density

Table 1 values of Al_2O_3 additive of 3Y-TZP + x wt% Al_2O_3 samples and their theoretical density values can be observed. The dental samples' density was determined through the Archimedes technique as outlined in ASTM C373 [57]. The theoretical density of the samples was calculated using the values of 6.1 g/cm^3 for 3Y-TZP [58] and 3.99 g/cm^3 for α-Al_2O_3 [58].

Table 1. Values of Al$_2$O$_3$ additive in 3Y-TZP+ x wt% Al$_2$O$_3$ dental samples and their theoretical density

Sample	3Y-TZP (wt.%)	Al$_2$O$_3$ (wt.%)	Theoretical density
x= 0	100.00	0.00	6.100000
x= 0.02	99.98	0.02	6.099800
x= 0.05	99.95	0.05	6.099173
x= 0.1	99.90	0.10	6.098346
x= 0.2	99.80	0.20	6.096692
x= 0.25	99.75	0.25	6.095865
x= 0.3	99.70	0.30	6.095038
x= 0.5	99.50	0.50	6.091730

3.3. Microstructural

The microstructure of polished surfaces treated at 1300 °C for 40 min in air and Pt-coated surfaces was analyzed using scanning electron microscopy (FESEM, Zeiss, Sigma 500). Grain size analysis was performed on SEM micrographs utilizing the linear intercept method, with a minimum of 1200 grains counted. The reported average results (± SD) were provided without any modifications [59]. The bulk density of the sintered samples was determined by applying Archimedes' principle, with measurements carried out in deionized water.

$$V_m = \frac{1.311 X_m}{1 + 0.311 X_m}$$

(12)

$$X_m = \frac{I_m(\bar{1}11) + I_m(111)}{I_m(\bar{1}11) + I_m(111) + I_t(101)}$$

(13)

where V_m represents the volume monoclinic phase, X_m indicates the proportion of the monoclinic phase relative to the total composition, I_m and I_t corresponds to the intensities of the diffraction peaks associated with m-ZrO$_2$ and t-ZrO$_2$ components, respectively.

Following the aging process, the aging time was used as a variable to illustrate the change

$$f_m = \frac{V_m}{V_{ms}} = 1 - \exp\left(-(bt)^n\right)$$

(14)

where f_m represents volume monoclinic fraction, V_m is monoclinic phase content, V_{ms} is the saturation of monoclinic phase, t is time, b (h^{-1}) is the kinetic parameter of phase transition, and n is the parameter associated with phase change structure factor [63].

3.5. Methods of Determining Mechanical Properties

3.4. Aging Kinetics

The LTD of various components was investigated by subjecting polished samples to water vapor at temperatures of 140 °C for different durations (0, 20, 30, 50, 80, 100, 200, 300, 500, and 800 h) using an autoclave (FCF-50 L, Zhengzhou Yuhua Instrument Manufacturing Co.). The transformation content of all specimens was analyzed using X-ray diffraction (XRD) with Cu-Kα radiation (50 kV, 45 mA) in the 2θ range of 29° to 32°, with a step size of 0.03 1/s. The volume fractions of m-ZrO$_2$ and t-ZrO$_2$ were determined from the diffraction patterns, following the methodology proposed by Toraya *et al.* [60] and Garvie and Nicholson [61] in equations 12 and 13:

curve of the monoclinic content. It is important to highlight that all samples exhibited XRD patterns between 20-80° (2θ) before aging, ensuring experiment precision. Additionally, to compare the aging kinetics across various doped ceramic samples, the transformation curves were fitted using the Mehl-Avrami-Johnson (MAJ) equation [62], as expressed in equation 14:

The Nanoindentation XP device from the Nanoinstruments Innovation Center (MTS systems, TN, USA) was utilized for nanoindentation experiments. Equipped with a Berkovich diamond indenter featuring a 50 nm tip radius, the tests presented data in the form of graphs showcasing the applied force (*P*) and penetration depth (*h*) throughout the loading and unloading phases [64]. In these experiments, a maximum load of 780 mN was applied, resulting

in a maximum penetration depth of around 1180 nm in the material. All tests were carried out at room temperature, with the system being calibrated using a fused silica standard prior to the experiments. Analyzing the force-depth curves derived from the nanoindentation tests, the hardness and Young's modulus (E) values of the samples were determined relative to penetration depth, with five measurements conducted for accuracy. For the analysis of the graphs, the nanoindentation test of the force component (P) varying with the indented depth component (h) during loading and unloading is plotted, and equations 15 to 17 are used [64]:

$$H_v = \frac{P_{max}}{A_c} \quad (15)$$

$$E = \frac{\sqrt{\pi}}{2\sqrt{A}} \times \frac{dp}{dh} \quad (16)$$

$$\frac{1}{Er} = \frac{(1-v^2)}{E} + \frac{(1-v_i^2)}{E_i} \quad (17)$$

These equations feature P_{max}, A_c, and H_v, which correspond to the maximum loading, contact area, and Vickers hardness, respectively. In addition, dp/dh represents the material stiffness, while E_r signifies the calculated modulus. A represents the area of all formed micro-cracks around the indented zone, v denotes Poisson's ratio, and the index i specifies the indenter. The Poisson's ratio and E of the diamond indenter (0.07 and 1140 GPa, respectively) are symbolized as v_i and E_i, whereas the sample's corresponding properties are denoted as v and E [64, 65]. Moreover, the Vickers microhardness test, ASTM E384 [66], was employed to evaluate and compare the hardness values. In this process, a Vickers diamond load equivalent to 98.06 N was exerted on each sample for 10 sec. The Vickers microhardness test took place in a controlled laboratory environment utilizing a Tukon 2100B hardness tester device, and the average hardness value for each sample was calculated based on seven measurements. In addition, the E of each sample was determined based on the variations in sonic velocity within the sample, as outlined in equation 18 of ASTM C769-98 [67]:

$$E = \rho v^2 \quad (18)$$

where ρ represents sample density and v is the speed of sound in the sample. This method involves transmitting and receiving a 5 MHz

ultrasonic pulse to and from each sample eight times to determine the speed of sound through the specimen by recording pulse times and measuring sample thickness. To determine Poisson's ratio of dental samples, equation 19 is used [65]:

$$H_v = 2\left(\frac{9E(1-2v)^2}{8(1+v)^3}\right)^{0.585} - 3 \quad (19)$$

where v is dimensionless, and H_v and E are expressed in GPa. During instrumented indentation testing, the Berkovich indenter is a popular choice because it shares a depth-to-area relationship with the four-sided Vickers pyramid commonly employed in micro-hardness evaluations. The Berkovich geometry stands out due to its three-sided pyramid shape, which can be sharpened to a point more effortlessly, retaining its self-similar geometry even at smaller scales.

In the analysis of the samples, K_{IC} values were acquired utilizing the single-edge laser-notch beam (SELNB) technique. This method involves the precision creation of an ultra-sharp V-notch on the samples using laser pulses. Subsequently, the fracture toughness of the samples is evaluated through three-point bending (TPB) tests, as detailed in [65]. To address the difficulties in machining a notch with precise depth and to prevent unintended crack formation, infrared ultra-short laser pulses were employed to create the ultra-sharp V-notch on the samples. The notches' depths varied from 80 to 120 μm, with a maximum tip radius of 2 μm. Given that the tip radius of the notch can impact the K_{IC} values, ensuring a sharpness of 2 μm was crucial to enhance result accuracy, as referenced in [58, 65, 68].

Figure 5 shows the created notch on the 3Y-TZP+ 0 wt% Al$_2$O$_3$ sample. It can be observed that the notch has appropriate geometry, and the absence of unintended damage indicates its quality and accuracy. The samples underwent testing using a TPB machine with a gauge length of 10 mm and a consistent displacement rate of 0.1 mm/min at room temperature. Figure 6 illustrates the schematic of the laser-notched sample for K_{IC} testing in the TPB test. Each sample underwent five SELNB tests, and the average values were recorded. equations 20 and 21 were applied in this method to determine the K_{IC} values, as described in reference [69].

$$K_{IC} = \frac{3L_s P_{max}}{2BW^{\frac{3}{2}}} . \alpha^{\frac{1}{2}} . Y^* \quad (20)$$

$$Y^* = \frac{(1.989 - 0.356\beta) - (1.217 + 0.315\beta)\alpha + (3.212 + 0.705\beta)\alpha^2 - (3.222 + 0.02\beta)\alpha^3 + (1.226 - 0.015\beta)\alpha^4}{(1-2\alpha)(1-\alpha)^{\frac{3}{2}}} \quad (21)$$

where P_{max} is the applied load at fracture, B represents the width of the specimen bar, W denotes the thickness of the specimen bar, α is the notched depth ($\frac{a}{W}$), Y^* is the stress intensity shape factor, and $\beta = \frac{W}{L_s}$.
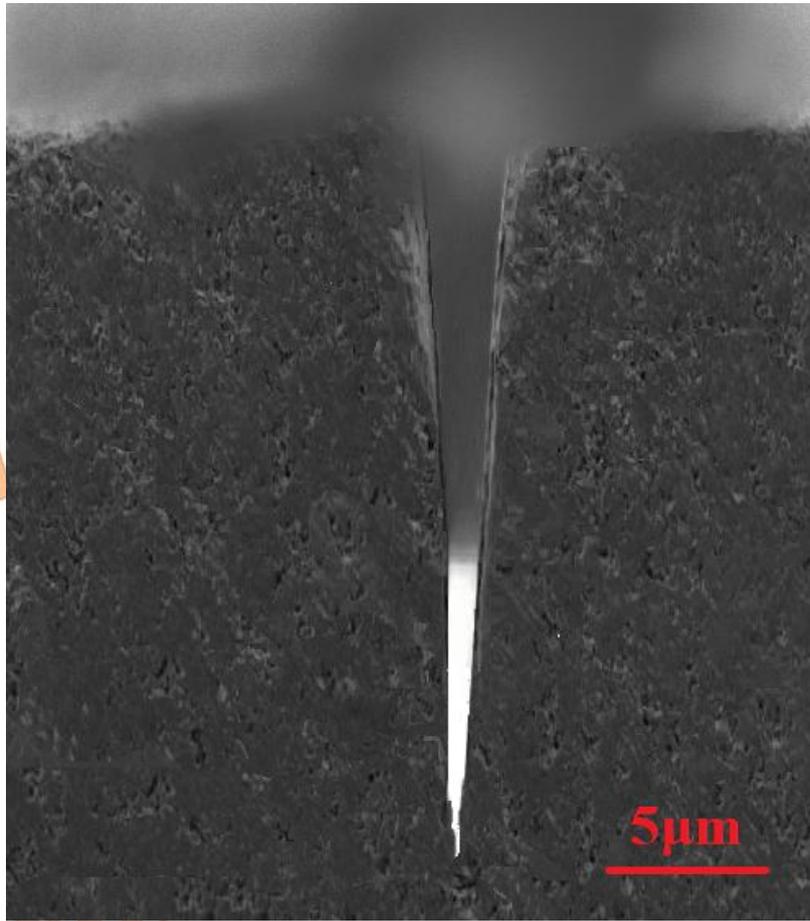

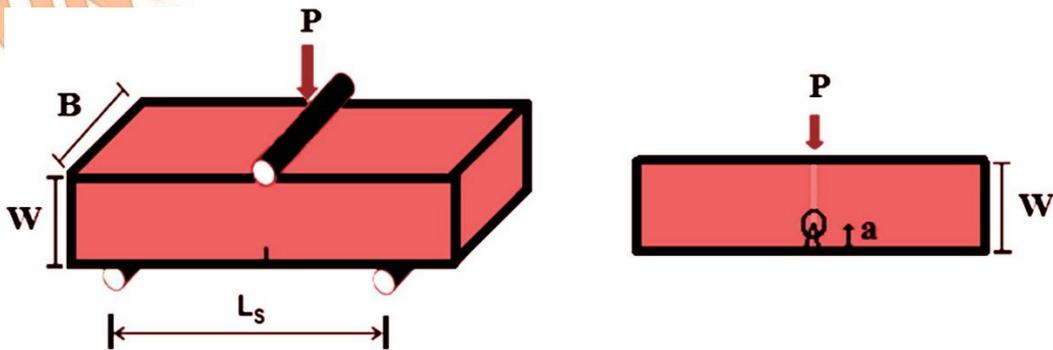**Fig. 5.** Laser-produced V-notch view in 3Y-TZP+ 0 wt% Al₂O₃ specimen

Fig. 6. Schematic of a Laser-notched plate dental sample in the SELNB test

The flexural strength (*MOR*) of the samples is determined using the TPB method ASTM C1161 [70] and calculated based on equation 22. Ten measurements are taken for each sample, and the average value is obtained.

$$MOR = \frac{3Fl}{2bd^2} \qquad (22)$$

where F represents the fracture force (N), l is the support span (m), b is the width of the sample (m), and d is the thickness of the sample (m).

4. Results and Discussion

4.1. Microstructure and Aging Resistance

The XRD pattern in Figure 7 displays the analysis of 3Y-TZP + x wt% Al₂O₃ ceramics after aging for 0 h and sintering in air at 1500 °C for 2

h. All eight 3Y-TZP/Al$_2$O$_3$ samples exhibited similar XRD patterns, showing distinct peak characteristics. The absence of monoclinic peaks (−111) m and (111) m at 2θ values of 28.3° to 31.4° was observed. In the 76–79° (2θ) range, the cubic phase peak (400) c was split into two peaks of the tetragonal phase, (004) t and (400) t. The presence of the characteristic (400) c peak and the cubic phase between the tetragonal (200) t and (002) t peaks was notably absent. Jade analyses indicated that the 3Y-TZP + x wt% Al$_2$O$_3$ ceramics (x= 0, 0.02, 0.25, 0.1, 0.2, 0.25, 0.3, and 0.5) comprised approximately 95% tetragonal phase and 5% monoclinic phase. This composition suggested that Al$_2$O$_3$ and Y$_2$O$_3$ had partially dissolved into the zirconia matrix, leading to Y$_3^+$ and Al$_3^+$ segregation at the grain boundaries, which is in line with established theories [71]. It is observed that increasing the proportion of the Al$_2$O$_3$ phase leads to an increase in the amount of monoclinic phase within the existing ZrO$_2$ structure. The highest quantity of monoclinic phase is attained in the 3Y-TZP sample without Al$_2$O$_3$.
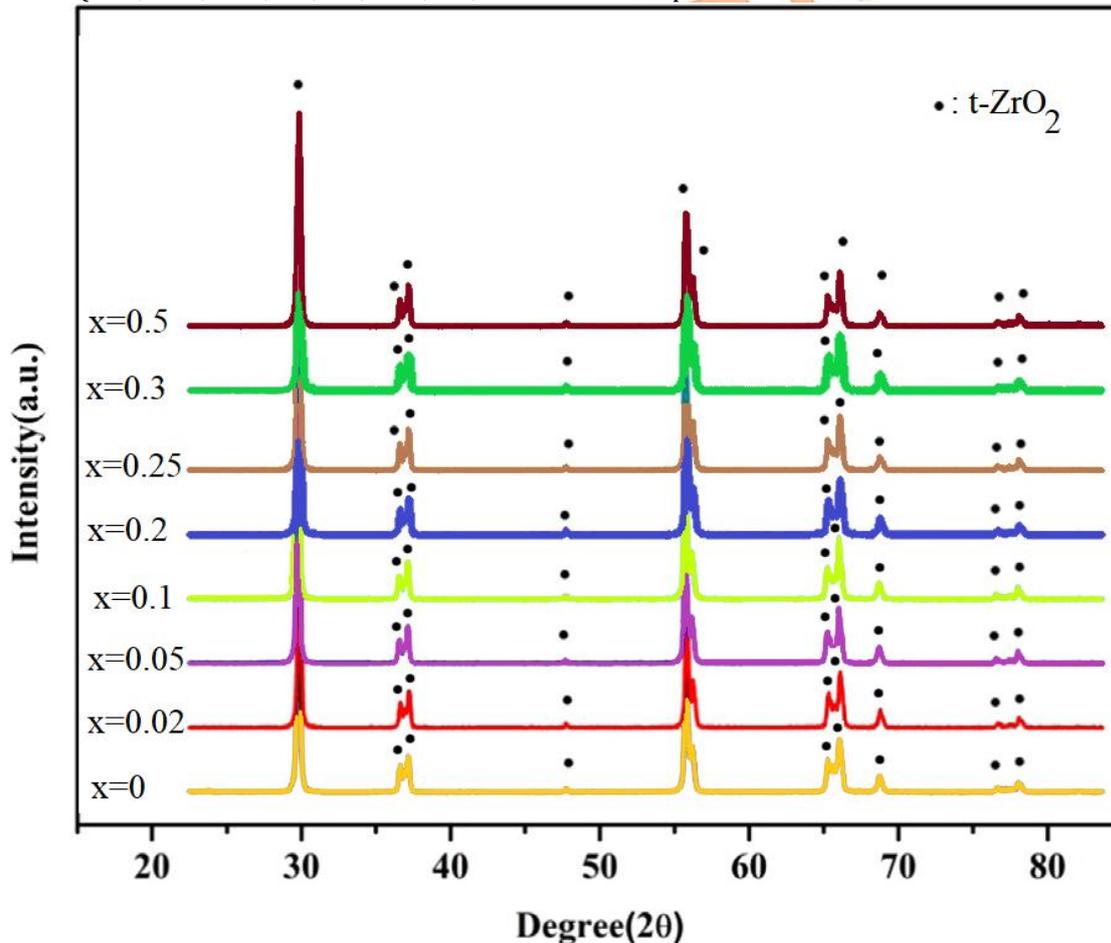

Fig. 7. XRD pattern of the 3Y-TZP + x wt% Al$_2$O$_3$ dental ceramics at 0 h of aging

Figure 8-a illustrates the surface monoclinic phase content of the 3Y-TZP + x wt% Al$_2$O$_3$ ceramics after sintering via a pressure-less method for 4 h at 1500 °C over a duration ranging from 0 to 800 h. In the case of 3Y-TZP ceramics doped with Al$_2$O$_3$, the content of m-ZrO$_2$ increases following the typical "S" curve pattern when plotted against the logarithm of aging time. This growth process can be divided into three main stages. Initially, there is a slow increase in monoclinic phase content with aging time, followed by a rapid escalation in the second stage, and ultimately reaching a saturation point in the third stage. Low-temperature aging leads to degradation, and the "S" shaped degradation observed in the ceramic material is a result of the isothermal transformation from the tetragonal to monoclinic phase. The hydrothermal stability improves with increasing Al$_2$O$_3$ content due to the enhancement of E, which hinders the growth of tetragonal phase ZrO$_2$ grains, contributing to stability. In addition, Al$_2$O$_3$ is more prone to hydrolysis than Y$_2$O$_3$, allowing for the formation of a protective matrix on the material surface. Figure 8-b illustrates the behavior of 3Y-TZP + x wt% Al$_2$O$_3$ ceramics, and by analyzing the corresponding plots of ln (ln (1/(1-f))) vs. ln(t) based on the data from (a) along with linear fittings, the parameter n in the MAJ Eq. 14 can be determined. Comparing experimental data with simulations, the exponent n for 3Y-TZP + x wt% Al$_2$O$_3$ ceramics falls within the range of 0.7 to 1.

Upon fitting the data from Table 2, the actual b (h^{-1}) value for the 3Y-TZP + x wt% Al_2O_3 ceramic was found to be 0.020 h^{-1}. This minimal b (h^{-1}) value indicates that Al_2O_3 doping can significantly reduce aging kinetics. Furthermore, the value of n increases from 0.7 to 1 with higher Al_2O_3 doping levels in dental ceramics. The value of n is associated with nucleation and growth during aging, where a smaller n value suggests dominant nucleation. The small experimental n value suggests the appearance of new nucleation sites during aging, hindering nucleus growth due to interactions with the new nucleation sites. Table 2 presents the values of MAJ Eq. parameters obtained through linear regression of monoclinic phase content against time, along with other relevant data for 3Y-TZP+ x wt% Al_2O_3 samples.
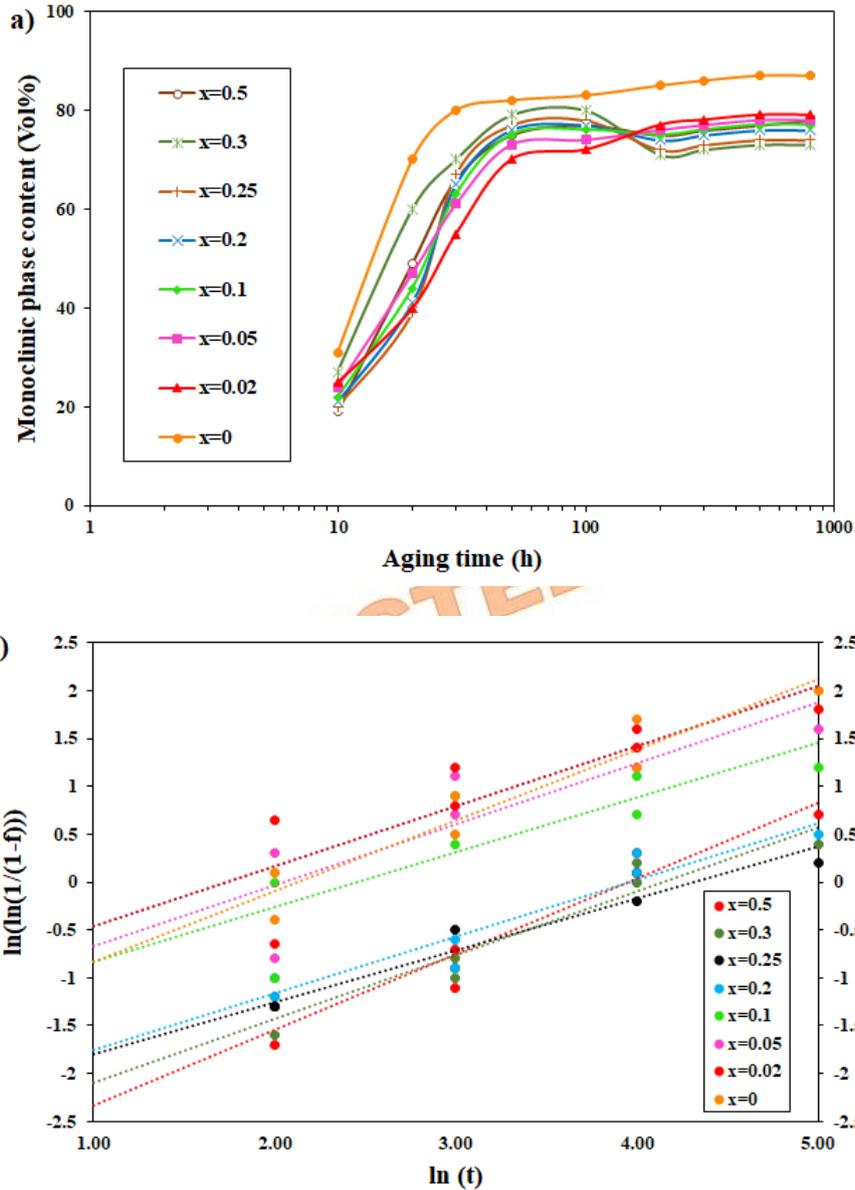

Fig. 8. (a) The percentage of surface monoclinic phase in the 3Y-TZP + x wt% Al_2O_3 ceramics after pressureless sintering for 3 hours at 1450 °C following 800 h of accelerated aging at 134 °C. (b) Representation of ln(ln(1/(1-f))) versus ln(t) for the 3Y-TZP + x wt% Al_2O_3 ceramics, based on the results in (a), including the linear regressions employed to calculate the parameter n in equation 14 of the MAJ model

Table 2. Parameters of the MAJ equation obtained through linear regression analysis of monoclinic phase content against time in 3Y-TZP+ x wt% Al_2O_3

Sample	c (Å)	V_{ms} (%)	n	b (h^{-1})
x= 0	5.2508	84.3	0.704 (0.121)	0.060 (0.014)
x= 0.02	5.2539	79.8	0.892 (0.124)	0.039 (0.007)
x= 0.05	5.2547	78.2	0.961 (0.122)	0.027 (0.005)
x= 0.1	5.2555	74.5	1.001 (0.119)	0.020 (0.003)
x= 0.2	5.2564	73.8	1.017 (0.129)	0.024 (0.009)
x= 0.25	5.2673	72.5	0.978 (0.125)	0.026 (0.004)
x= 0.3	5.2681	71.2	0.969 (0.124)	0.027 (0.005)
x= 0.5	5.2689	70.2	0.964 (0.125)	0.029 (0.003)

Figure 9 showcases typical FESEM images of the sintered 3Y-TZP + x wt% Al_2O_3 ceramics, revealing a consistent microstructure across all samples. The specimens display a compact polygonal matrix with well-defined grain boundaries. With higher Al_2O_3 concentrations, the grain size shows enhanced uniformity, with the smallest and most homogeneous grain size observed at an Al_2O_3 doping level of 0.25 wt%. Table 3 summarizes the relative density, average grain diameter, and average porosity size of the 3Y-TZP + x wt% Al_2O_3 ceramics sintered at 1500 °C in air for 2 h.

Table 3. Rietveld analysis results on the phase composition, lattice parameters, relative density, average grain and average porosity diameter in 3Y-TZP+ x wt% Al_2O_3 dental ceramic samples

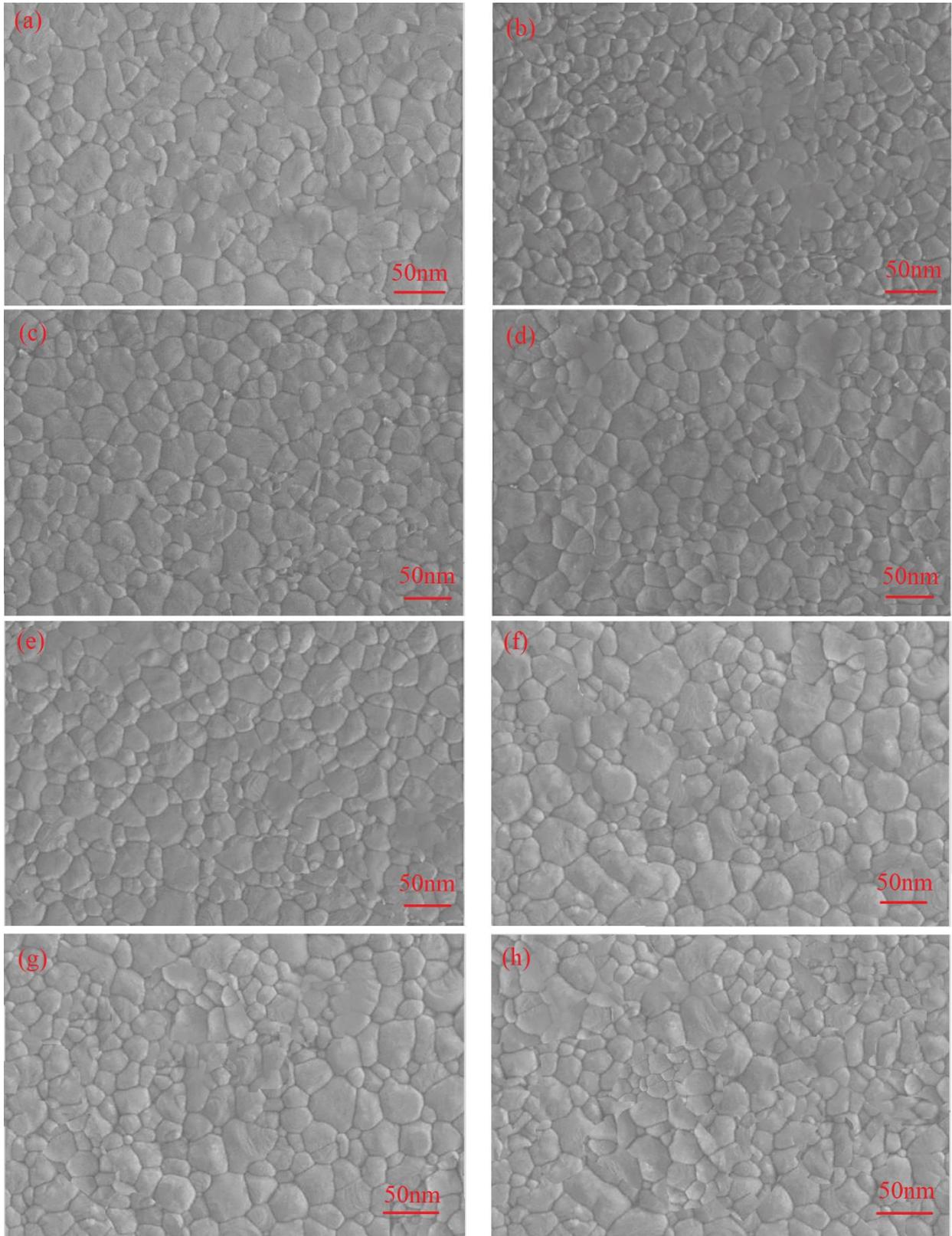| Sample	Y_2O_3 (mol%)	Relative density (%)	Average grain (nm)	Average porosity diameter (nm)
x= 0	2.75	97.4 ± 0.5	89	10
x= 0.02	2.80	98.1 ± 0.6	85	9
x= 0.05	2.80	98.3 ± 0.4	92	10
x= 0.1	2.80	98.7 ± 0.4	100	12
x= 0.2	2.80	99.1 ± 0.3	104	11
x= 0.25	2.85	99.2 ± 0.4	106	8
x= 0.3	2.80	99.3 ± 0.4	78	11
x= 0.5	2.75	99.5 ± 0.4	80	10

Fig. 9. FESEM micrographs of 3Y-TZP+ x Al$_2$O$_3$ dental ceramics (a) x= 0, (b) x= 0.02 (c) x= 0.05 (d) x= 0.1 (e) x= 0.2 (f) x= 0.25 (g) x= 0.3 (h) x= 0.5

4.2. Mechanical Properties

Figure 10 showcases the load-displacement (*p-h*) curves obtained from the nanoindentation test performed on the plate samples. Figures 11 and 12 present the hardness (*H*) and Young's modulus (*E*) values of the 3Y-TZP+ x wt% Al$_2$O$_3$ samples, respectively, relative to the penetration depth. Beyond a penetration depth of 120 nm, the E and H values of all samples remain relatively constant regardless of the penetration depth. As

per equation 18, E is directly linked to density; hence, a decrease in density, resulting in increased porosity, also leads to a decrease in Young's modulus. Comparing the reported Young's modulus values for ZrO_2 ($E \approx 250$ GPa) [72] and Al_2O_3 ($E \approx 380–500$ GPa) [73–77], and noting the significant disparity between them, the critical particle size can potentially be raised to around 1 mm; whereas, for a microstructure comprising 100% 3Y-TZP phase, this critical size is approximately 0.3 mm [78]. By enhancing the proportion of the additive phase and lowering E of resultant dental ceramics, thereby alleviating the constraints imposed by the matrix and critical size parameters, the tetragonal phase content is reduced. It is also evident that the relative densities of samples have increased with the rise in the additive phase percentage. This augmentation in relative density may be attributed to the disparate thermal expansion coefficients of the two materials, resulting in the appearance of porosity in the specimens' microstructures. Furthermore, elevating the sintering temperature enhances the relative density of the samples, potentially due to the improved sinterability of the specimens. All ceramic samples demonstrated high density and hardness, with the fracture toughness of 3Y-TZP + x wt% Al_2O_3 exceeding 10.07 $MPam^{1/2}$. This value represents a 0.9 improvement compared to similar dental ceramics in another study [79].

In the case of all ceramics prepared using the precipitation method for powder production, some Y_2O_3 dissolved into the ZrO_2 lattice during the titration process (See Table 3). Therefore, from a sintering perspective, all sample ceramics underwent a single sintering synthesis. The non-uniform distribution of Y_2O_3 within the samples resulted in the segregation of a small quantity of Y_2O_3. This segregation helped disperse residual stress, strengthen the grain boundary, and impede grain growth [80]. The H_v, E, K_{IC} and flexural strength values of specimens are shown in Table 4. In the realm of zirconia-based ceramics, two established toughening mechanisms are widely recognized. These mechanisms encompass toughening via a phase transition and ferroelastic toughening associated with the non-transition tetragonal phase [81, 82]. Within the framework of the toughening mechanism, when an external force of significant magnitude is applied, the metastable tetragonal phase of the ceramic material undergoes a transition to the monoclinic phase. This phase transformation generates compressive stress at the crack tip, which helps in absorbing a portion of the fracture energy. Therefore, the crack propagation is impeded, and further growth of the crack is prevented. This mechanism plays a crucial role in enhancing the fracture toughness and durability of zirconia-based ceramics [71, 83, 84].
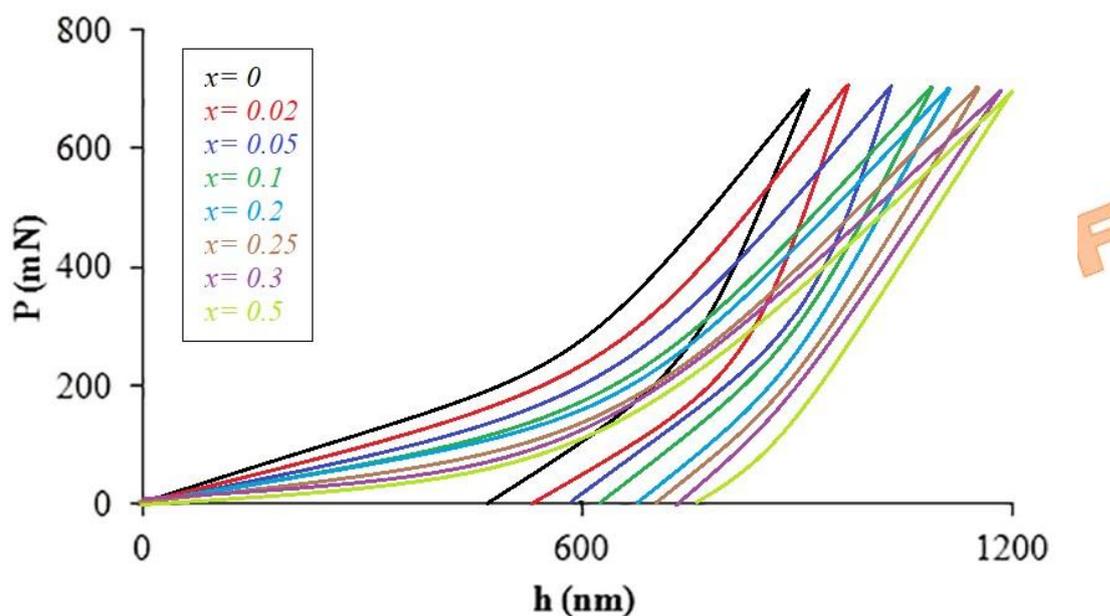

Fig. 10. Nanoindentation test results displaying the load-displacement (*P-h*) curves for dental plate samples of 3Y-TZP+x Al_2O_3
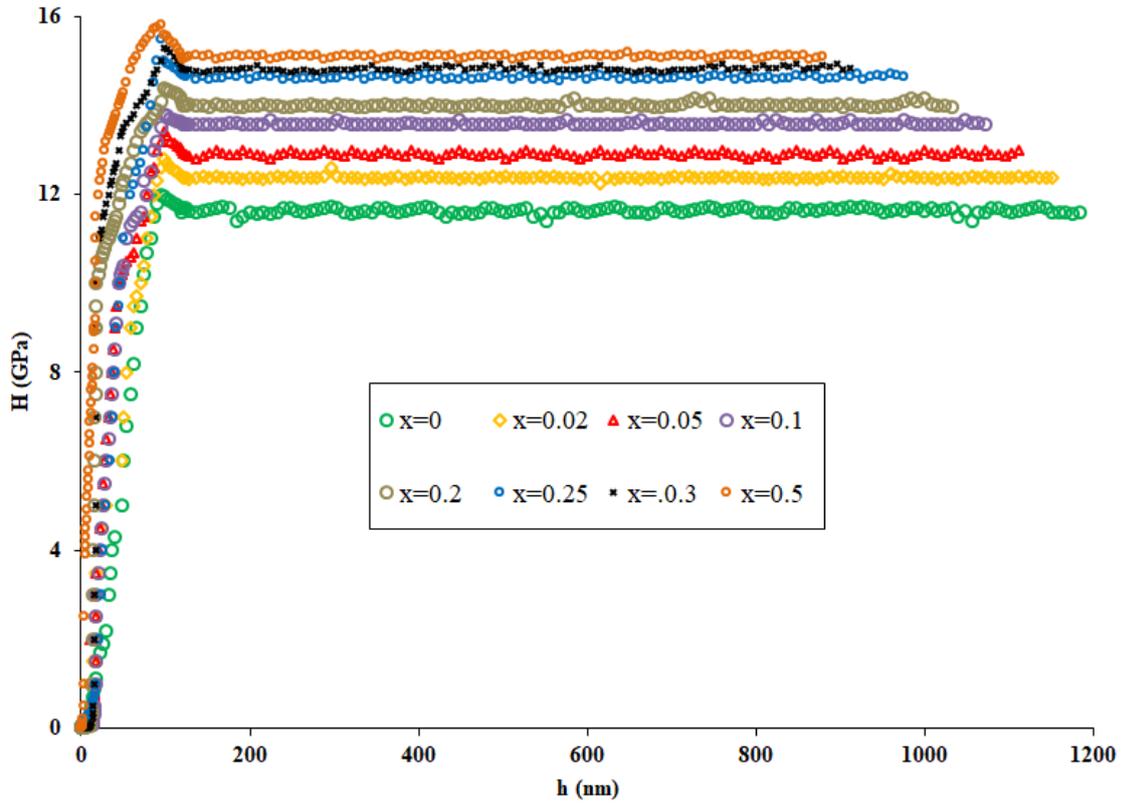
Fig. 11. Nanoindentation test results show the hardness-displacement (*H-h*) curves for dental plate samples of 3Y-TZP+x Al$_2$O$_3$
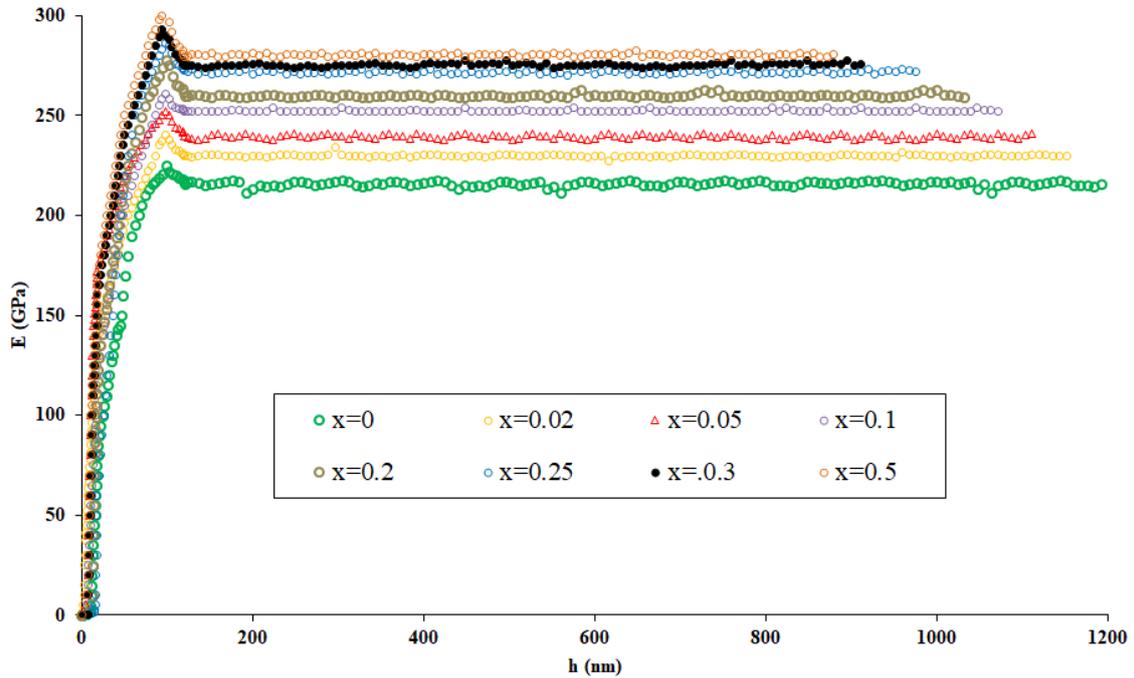

Fig. 12. Nanoindentation test results illustrate Young's modulus-displacement (*E-h*) curves for dental plate samples of 3Y-TZP+x Al$_2$O$_3$

Table 4. Hardness (GPa), Vickers hardness (GPa), Young's modulus (GPa), Poission's ratio, Fracture toughness (MPa.m$^{1/2}$), and Flexural strength (MPa) values of 3Y-TZP+ x wt% Al$_2$O$_3$ dental plate ceramics

Sample	Nanoindentation method		Vickers Hardness indentation (GPa)	E: according to sonic velocity (GPa)	Poisson's ratio (v)	Fracture toughness (MPa.m$^{1/2}$)	Flexural strength (MPa)
	H (GPa)	E (GPa)					
x= 0	11.63± 0.33	216 ± 6.2	11.48± 0.04	211 ± 3.2	0.34	9.48 ± 0.20	312 ± 7
x= 0.02	12.38 ± 0.35	230± 6.5	11.87 ± 0.08	218 ± 6.4	0.34	9.53 ± 0.06	318 ± 6
x= 0.05	12.90 ± 0.19	240 ± 3.6	12.36 ± 0.03	232 ± 5.9	0.33	9.66 ± 0.10	321 ± 9
x= 0.1	13.59 ± 0.10	252 ± 1.9	12.78 ± 0.01	239 ± 8.3	0.32	9.72 ± 0.08	319 ± 8
x= 0.2	14.01 ± 0.21	260 ± 3.7	13.03 ± 0.02	247 ± 2.1	0.31	9.81 ± 0.07	328 ± 4
x= 0.25	14.64 ± 0.16	272 ± 3	13.33 ± 0.03	256 ± 5.7	0.30	9.91 ± 0.11	336 ± 5
x= 0.3	14.83 ± 0.20	275 ± 3.6	13.61 ± 0.02	261 ± 4.8	0.29	9.94 ± 0.09	339 ± 6
x= 0.5	15.10 ± 0.17	280 ± 3.2	14.21 ± 0.03	274 ± 9.5	0.27	9.97 ± 0.10	355 ± 7

4.3. Effect of Nanoporosity on Dynamic Fracture in TPB Test

PD simulations have been carried out to examine how Young's modulus, density, Poisson's ratio, and fracture energy affect crack behavior when nanoporosities are present. Furthermore, the study delves into how the sizes of these nanoporosities impact the propagation of macro-cracks and the phenomena of crack arrest. Moreover, the analysis explores the impact of various velocity boundary conditions (BCs) on the path of the crack and its propagation speed. The appropriate time step size (Δt) must be determined to ensure a stable solution. In quasi-static problems, the adaptive relaxation technique is utilized to achieve a steady-state solution, and a time step size of $\Delta t = 1$ is used [54]. For dynamic problems involving propagating cracks, a stability criterion for Δt has been

introduced [53]. Given that the stable time step size is contingent on the horizon size ($\delta = 3.018$ Δx) and affected by the mass density of the 3Y-TZP/Al$_2$O$_3$, all dynamic computations on dental plates are executed utilizing $\Delta t = 0.05$ µs.

In Figure 13-a, a dental plate with dimensions is described as follows; length (L) = 0.2 m, width (W) = 0.05 m, and thickness (h) = 0.05 m. The dental plates are subjected to TPB loading, with supports located at a distance (L_s) of 0.1 m from each other. At the bottom edge of the dental plate, there is a pre-existing crack with a length of $2a$ = 0.004 m. The material properties of the dental plates are described in Tables 3 and 4 for each sample. The dental plates are constrained by displacement, with $v(x, y = W, t)$ set at 2.5×10^{-3} m, and have fixed supports at $y = 0$. The boundary conditions are implemented according to equations 23-26 [26]:

$$u_f\left(x_f, y_f, t+\Delta t\right)=0 \text{ at } -2\Delta x \leq x \leq 2\Delta x \qquad x_f \in -2\Delta x \leq x \leq 2\Delta x \tag{23}$$

$$v_f\left(x_f, y_f, t+\Delta t\right)=-v\left(x, y, t+\Delta t\right), \ W \leq y \leq W+\delta \qquad y_f \in W \leq y \leq W+\delta \tag{24}$$

$$u_{f_s}\left(x_{fs}, y_{fs}, t+\Delta t\right)=0 \tag{25}$$

$$v_{f_s}\left(x_{fs}, y_{fs}, t+\Delta t\right)=0 \tag{26}$$

In Figure 13-b, the displacement boundary conditions are enforced at the fictitious region R_f, situated in the central part of the top edge of the plate. The PD model is discretized using 5×10^5 material points with evenly distributed spacing between them ($\Delta x = 6 \times 10^{-9}$ m), and a horizon size of $\delta = 3.018 \ \Delta x$. To achieve the quasi-static loading condition, a total of 3×10^3 time steps are used with the adaptive dynamic relaxation method, and the time step size is set to $\Delta t = 1$s [54]. The fixed displacement and velocity

boundary conditions are rigorously established in the fictional region R_{fs} at the bottom of the plate. The width of the R_{fs} regions precisely aligns with the horizon size of $\delta = 3.018 \ \Delta x$. Comparisons between the PD and FEM results are meticulously examined and graphically depicted in Figures 14 and 15. Impressively, the PD findings for displacements along the central lines of the dental plates showcase remarkable consistency with the FEM outcomes.
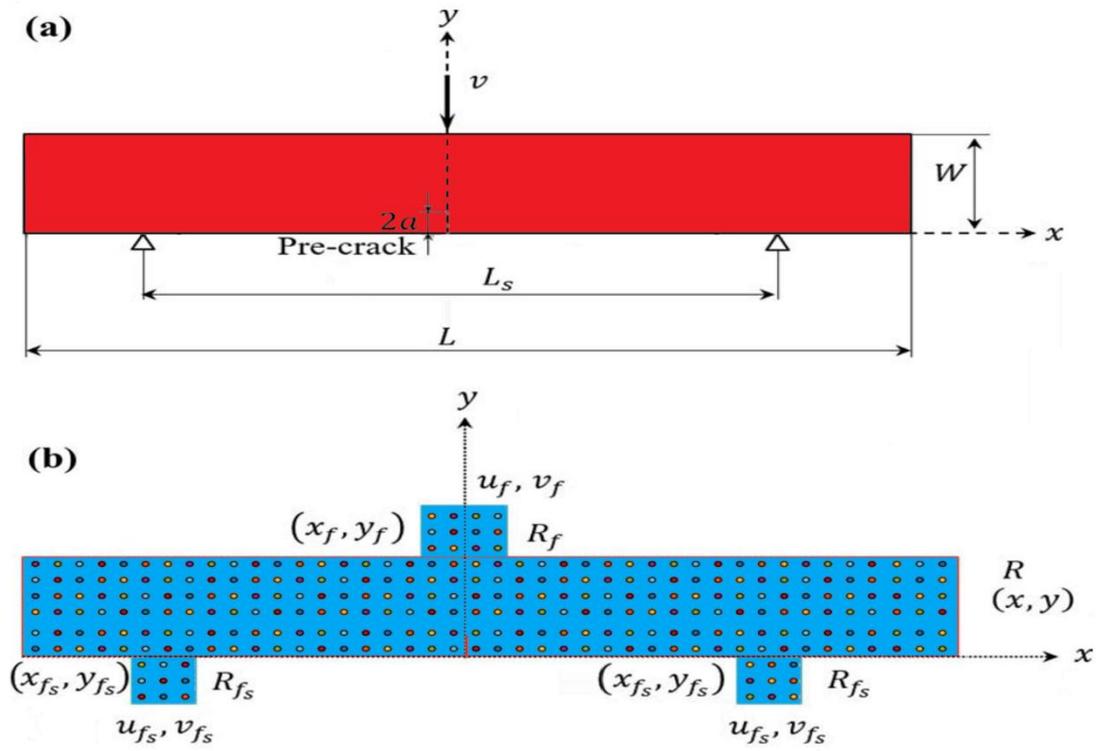
Fig. 13. a) Schematic of a pre-cracked dental plate in bending loading b) its discretization
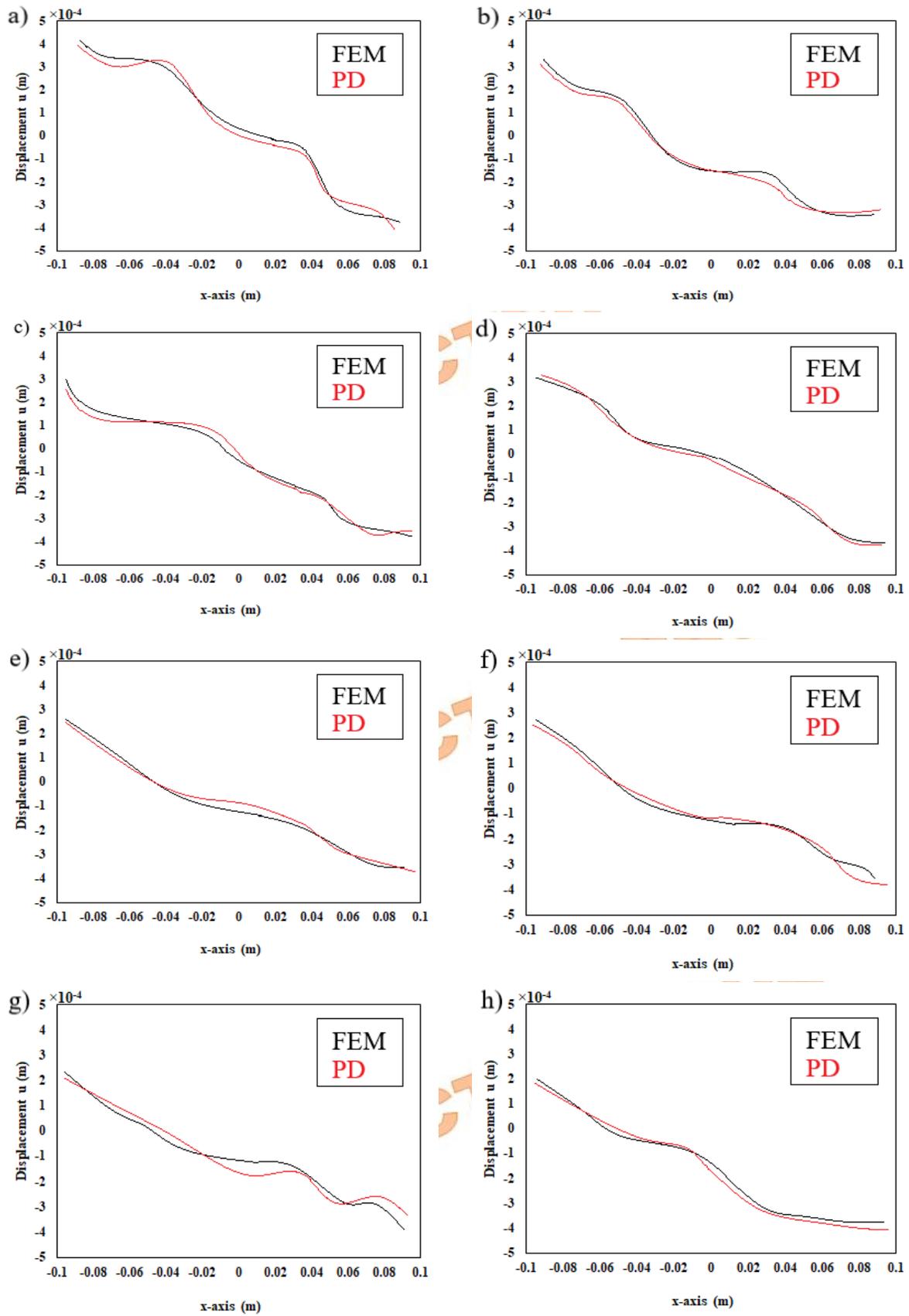
17

Fig. 14. Variations in displacement along the center lines in 3Y-TZP + x Al$_2$O$_3$ samples at u (x, y = 0) a) x=0 b) x=0.02 c) x=0.05, d) x=0.1 e) x=0.2 f) x=0.25 g) x=0.3 and h) x=0.5 wt%
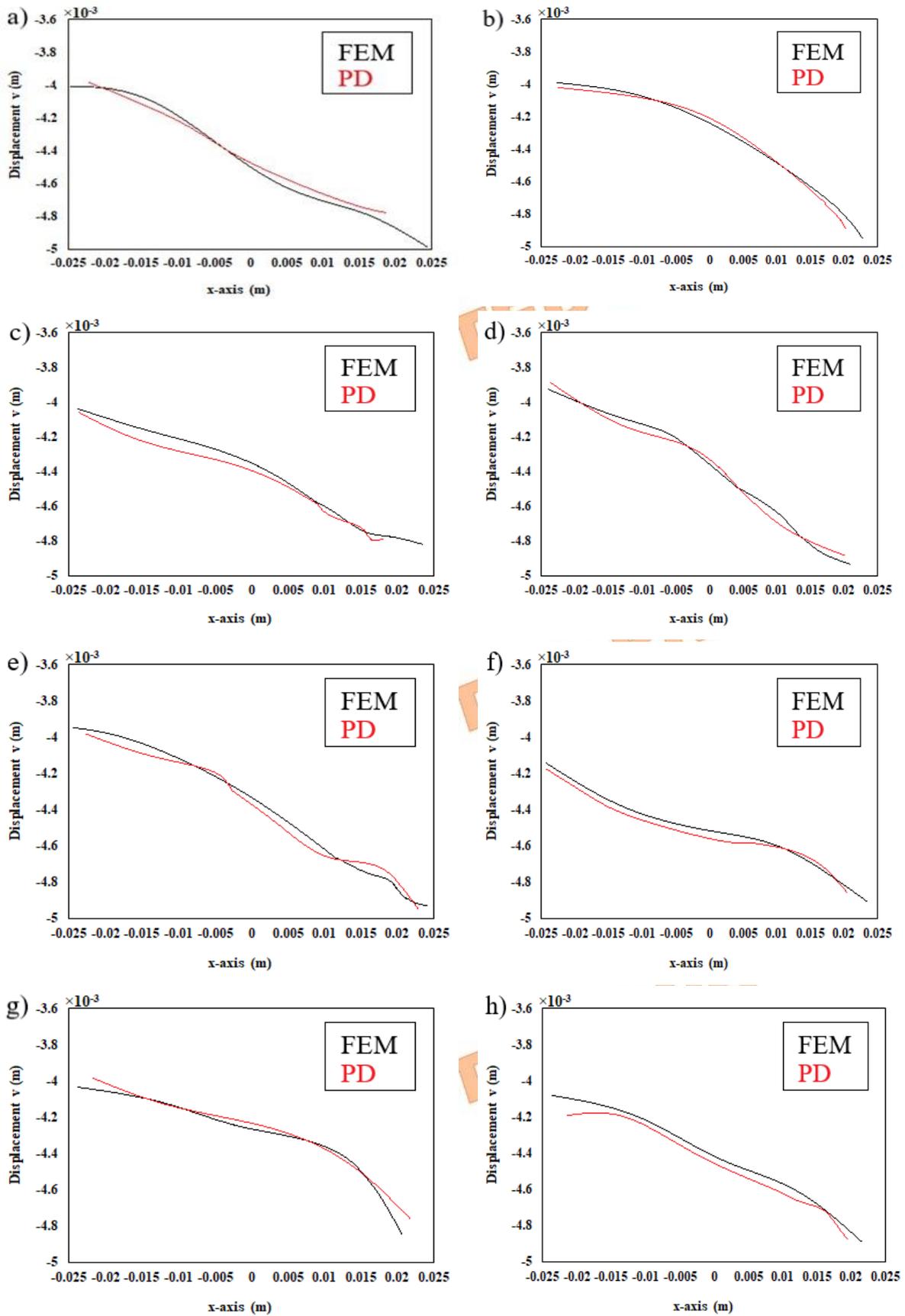
Fig. 15. Variations in displacement along the center lines in 3Y-TZP + x Al$_2$O$_3$ samples at v ($x = 0, y$) a) x=0 b) x=0.02 c) x=0.05, d) x=0.1 e) x=0.2 f) x=0.25 g) x=0.3 and h) x=0.5 wt%

According to the experimental results, the samples containing 0.1 wt% Al_2O_3 exhibit the highest porosity. In Figure 16, the pre-crack in the three-point test spans a length of $2a = 0.005$ m and is positioned at the lower edge of the plate. Following the identification of maximum porosities in the samples, an in-depth investigation is initiated. Noteworthy is the placement of the nanoporosity at a specific distance of $dx = 0.005 + R$ m and $dy = 0.03$ m from the origin of the main coordinate system, which is anchored at the base of the crack. Velocity boundary conditions of (a) $\dot{v} = 1$ m/s and (b) $\dot{v} = 4$ m/s are applied at the fictitious region located on the top edge of the plate, as visually represented in Figure 13-b, according to equations 27 and 28 [26].
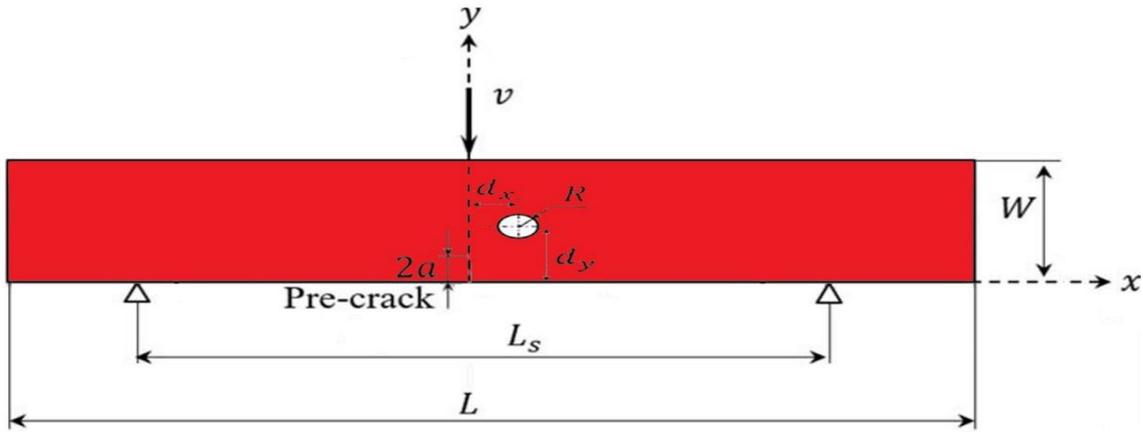
$$u_f\left(x_f, y_f, t+\Delta t\right)=0 \quad \text{at} \quad -2\Delta x \leq x \leq 2\Delta x \qquad x_f \in -2\Delta x \leq x \leq 2\Delta x \tag{27}$$

$$v_f\left(x_f, y_f, t+\Delta t\right)=-\dot{v}\left(x, y, t+\Delta t\right)\times \Delta t \;,\; W \leq y \leq W+\delta \qquad y_f \in W \leq y \leq W+\delta \tag{28}$$

Fig. 16. Schematic of a pre-cracked dental plate with a nanoporosity in bending

Discretized with 1.6×10^8 material points spaced uniformly at $\Delta x = 6\times 10^{-9}$ m, the PD models have a defined horizon size of $\delta = 3.018 \Delta x$. Employing a consistent time step size of $\Delta t = 0.081$ μs, the simulation includes a critical stretch of $Sc = 0.01072$, corresponding to an energy release rate of $G_0 = 220$ J/m^2. The crack propagation behavior under varied loading conditions is depicted in Figure 17 as analyzed through PD. When the structure is devoid of any porosity, the crack propagation follows a self-similar pattern. In contrast, with the presence of porosities within the structure, the crack path undergoes a noticeable shift and veers towards the porosities. This is consistent with the observed crack propagation pattern in the experimental tests [85]. In addition, larger holes result in a higher deflection of the crack, The crack path deviates towards the defect upon its approach, returning to its original trajectory after propagating nearby. The crack trajectory appears curved and symmetric concerning the local axis of the porosity. Under both velocity boundary conditions, the crack advances towards the porosity, halts momentarily at its edge without intersecting, and subsequently proceeds towards the designated position of the applied boundary condition. To evaluate and calculate the crack propagation speed according to equation 29 [26]:

$$V = \frac{x_p - x_{p-1}}{t_p - t_{p-1}} \tag{29}$$

where the current crack tip position (t_p) is indicated as x_p, while the previous crack tip position (t_{p-1}) is denoted as x_{p-1}.
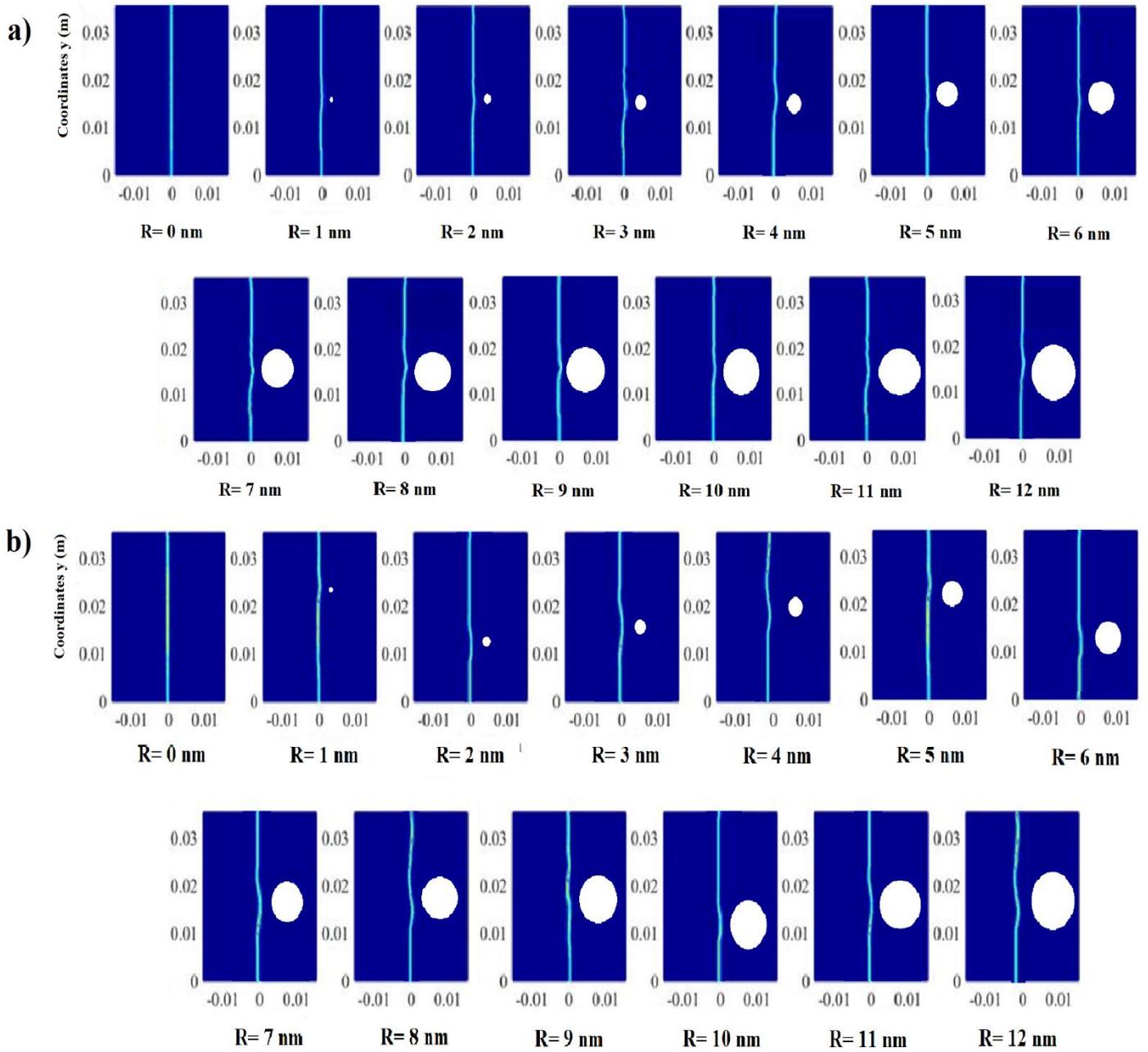
Fig. 17. PD Damage maps of 3Y-TZP+ x Al$_2$O$_3$ dental plates with varying porosity radius R and under velocity boundary conditions: a) $\dot{v}$ =1 m/s at t = 480 μs, b) $\dot{v}$ =4 m/s at t = 280 μs

In Figure 18-a, the diagram shows the relationship between crack propagation speed and crack growth. Initially set at $\dot{v}$ = 1 m/s, the speed increases to V = 400 m/s as the crack tip nears a nanoporosity with a radius of R = 6×10^{-9} m at coordinates x = 0 m and y = (dy - 0.02) m. As the crack advances towards the nanoporosity, its propagation speed diminishes gradually, hitting a low point at V = 200 m/s when the crack tip is positioned at x = 6 × 10^{-4} m and y = dy + 0.025 m. Subsequently, there is a brief pause in the crack propagation, lasting about 10 μs, before the crack resumes its original course with an accelerating speed, as illustrated in Figure 18-b. The trend

remains consistent with a higher velocity BC of $\dot{v}$ = 4 m/s, as depicted in Figure 18-a. In this scenario, the crack propagation speed escalates, peaking at V = 600 m/s. As the crack approaches the porosity, it veers towards it while the speed gradually decreases, reaching V = 400 m/s. The crack also curves towards the porosity with a decreasing speed to V = 400 m/s. After a very short crack arresting period of 3 μs (Figure 18-b), the crack recovers and continues to propagate away from the porosity with an increasing speed. The phenomenon of crack arrest has been observed in multiple tests, and it is similar to the results obtained from PD simulations. However,

21

detecting crack arrest is challenging as the arrest period is very brief. Furthermore, it is observed that the occurrence of crack arrest is dependent on the applied force, as shown in Figure 18-b. A lower velocity BC results in a longer delay in crack propagation. In addition, Figure 18-c illustrates the findings regarding crack propagation speed and time when applying a velocity boundary condition of $\dot{v} = 1$ m/s to a plate containing a nanoporosity with a radius of $R = 6\times10^{-9}$ m. Significantly, a clearly defined crack

arrest phase, lasting approximately 13 μs, initiates at $t = 138$ μs coinciding with the crack tip position at $dy = 0.003$ m. Concurrently, the crack propagation speed decreases to $V = 130$ m/s before returning to its original pace. A potential explanation for the more distinct crack arrest phase could be the predominant linear propagation of the crack, with minimal deviation towards the porosity, as visualized in Figure 17-a for $R = 6\times10^{-9}$ m.
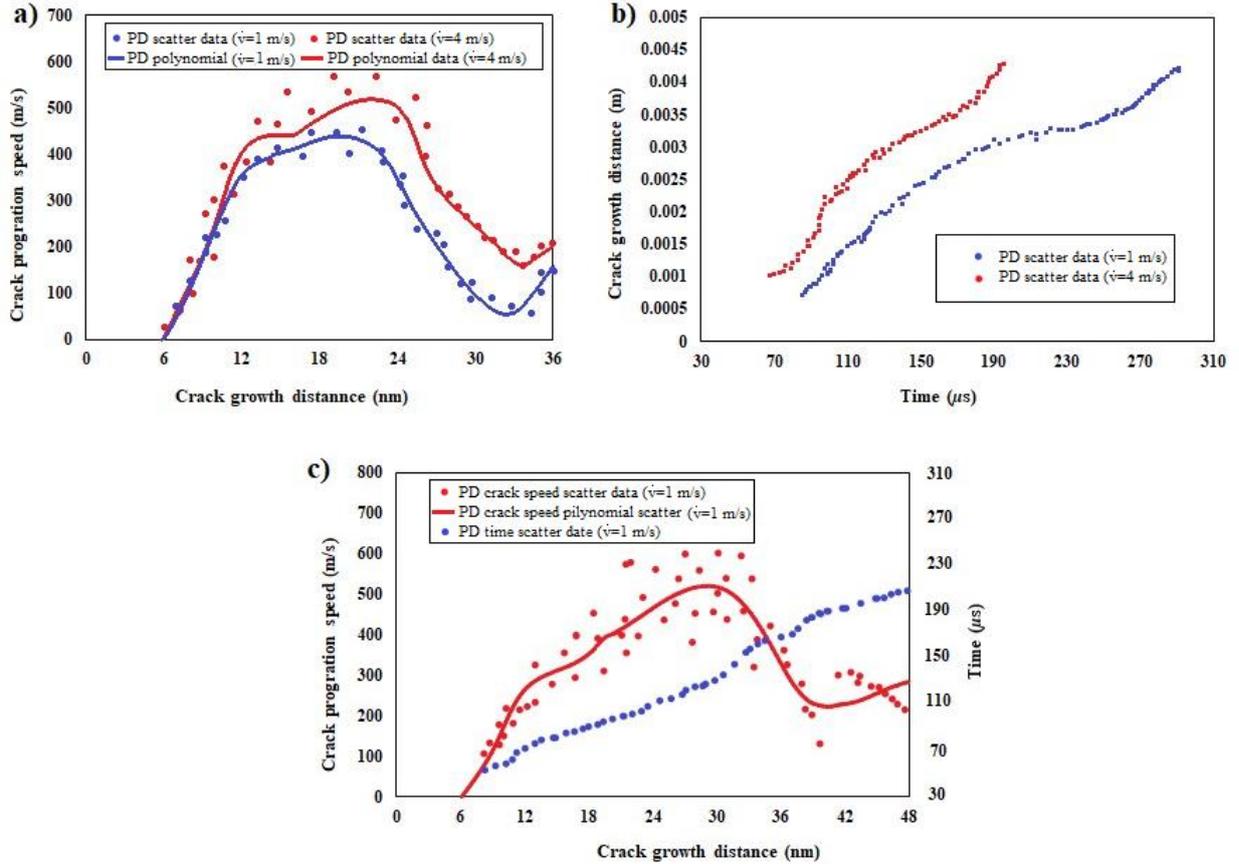

Fig. 18. Behavior of a dental plate ceramics sample with 3Y-TZP+ 0.5wt% Al$_2$O$_3$, porosity radius $R = 12$ nm, under velocity boundary conditions of $\dot{v} = 1$ m/s and $\dot{v} = 4$ m/s. a) Crack propagation speed vs. growth distance. b) Crack length evolution over time. c) Crack propagation speed, time, and growth distance for $R = 6$ nm under $\dot{v} = 4$ m/s
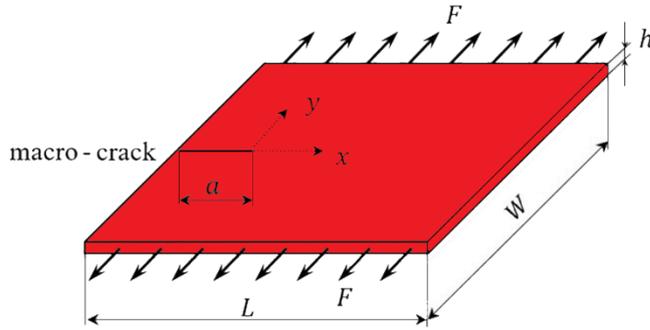
4.4. Influence of Micro-cracks on Macro-crack Propagation in Stress-Loaded Dental Ceramic Plate

The geometric parameters influencing the interaction between macro- and micro-cracks include crack dimensions, distances between micro-cracks, and their orientation. In the PD model outlined in the study, a macro-crack with dimensions $a = 0.055$ m is situated on the left side of the plate, as depicted in Figure 19-a. Furthermore, the model encompasses five distinct scenarios involving distributed micro-cracks, each with a length of $a_c/a = 0.15$. The micro-cracks distances are represented by a/s and a/r, with $s = r = 2$. These micro-cracks are

situated around and in front of the macro-crack tip, as shown in Figure 20. The configurations of the micro-cracks are analyzed for cases (a) to (e), with the crack inclination angle α varying from 0°, 45°, to 90° in each scenario. The micro-cracks are positioned in a regular manner within the +y and/or -y domains and in front of the main crack tip. Geometric parameters for the 3Y-TZP/Al$_2$O$_3$ plate consist of a length (L) of 0.2 m, width (W) of 0.33 m, and thickness (h) of 0.005 m. The material properties include an elastic modulus of 250 GPa and v of 0.3. Quasi-static PD simulations are carried out using an explicit time integration scheme with a stable time step size of $\Delta t = 1$, incorporating the adaptive relaxation technique [54]. During dynamic PD simulations, a time step size of $\Delta t = 0.2$ μs is utilized [53]. The stability

criterion for the dental plate differs as it depends on the horizon size ($\delta = 3.018\ \Delta x$), with the spacing between points set at $\Delta x = 12 \times 10^{-9}$ m instead of the previously used $\Delta x = 6 \times 10^{-9}$ m.
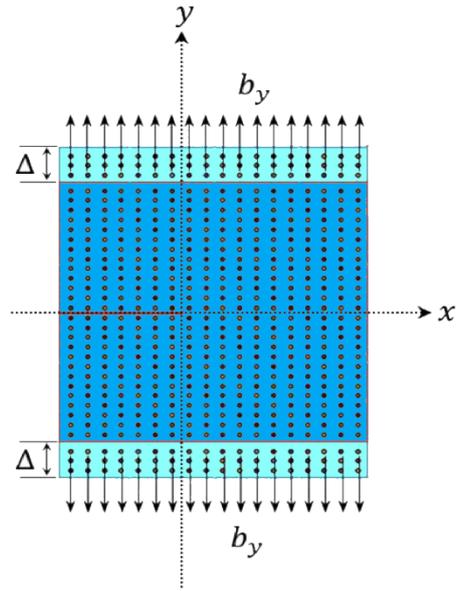
(a)

(b)

Fig. 19. a) Dental plate with a macro-crack in quasi-static loading b) Discretization of the dental plate with a macro-crack in body force density boundary conditions, following the model by Karpenko *et* al. [26]

4.5. Critical Load for Dental Plates with Micro-cracks

The aim is to investigate how micro-cracks ahead of the macro-crack tip impact its propagation. Five different models of micro-crack distributions are studied, as displayed in Figure 20. The dental plate is under symmetric quasi-static compressive loading in the y-direction, as depicted in Figure 19-a. After conducting a convergence study, it was established that employing 3000 time steps with a time step size of $\Delta t = 1$ s is effective for achieving quasi-static loading conditions using the adaptive dynamic relaxation method [29]. Initially, a load of $F = 100$ N is applied, leading the system to a steady-state solution. Then, the applied force is incremented by $\Delta F = 1$ N after every 3000 time steps. The evaluation involves assessing the elongation of bonds between material points. When the elongation surpasses the critical elongation threshold ($s > s_c$), the applied force is recognized as the critical load p. These critical loads are labeled as p^0 for a dental plate featuring a single macro-crack and p^* for the plate with both a macro-crack and distributed micro-cracks. The PD model is discretized using 118,520 material points, as illustrated in Figure 19-b. The material points are uniformly spaced with a distance of $\Delta x = 10 \times 10^{-9}$ m. Moreover, the horizon parameter δ is established at 3.018 times the value of Δx. To replicate the loading scenario, a quasi-static loading condition is imposed through a body force density, as described in equation 30 [26].

$$b_y = \frac{F}{\Delta_{V_\Delta}} \tag{30}$$

where the volume of the boundary layer is represented by ΔV_Δ, with a specific value set at $\Delta V_\Delta = 1.98 \times 10^{-6}$ m³. The PD numerical models are under investigation to explore the connection between the SIF of the case featuring a macro-crack, labeled as K_0, and those scenarios involving micro-cracks, denoted as K^*. Throughout this analysis, a uniform fracture energy value of $G_0 = 560$ J/m² is considered across all cases. The numerical model undergoes assessment using a consistent critical stretch-based criterion, where $s_c^* = s_c = 0.0048$, applied to all five instances of micro-crack distributions, as well as to the scenario with only one macro-crack featuring s_c^*. It is important to highlight that the critical stretch remains unaffected by the micro-crack layouts or the varying crack inclination angles α, ranging from 0°, 45°, and 90°.
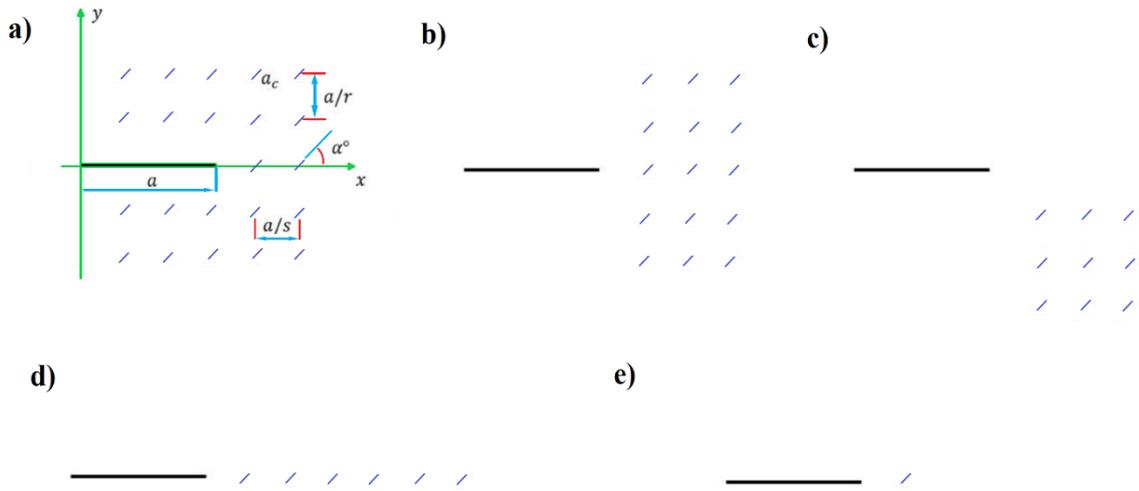
23

Fig. 20. Different arrangements of micro-crack distributions: a) Micro-cracks encircling the main crack tip, b) Micro-cracks positioned ahead of the crack tip, c) Uneven distribution of micro-cracks (+y domain) in front of the main crack tip, d) Cluster of micro-cracks located in advance of the crack tip, e) Solitary micro-crack positioned in front of the main crack tip

The PD simulations have been executed, with the outcomes depicted in Figure 21. The study involved assessing the ratios of critical loads, p^* and p^0. It was noted that the impact of micro-cracks on crack propagation aligns with the anticipated pattern from analytical solutions [34]. Nonetheless, the analytical findings revealed lower ratios of critical loads for inclination angles spanning from 0° to 45° when compared to the results derived from PD simulations. The discrepancy can be linked to the uniform critical stretch utilized in the PD simulations. Chen and Chu [86] offer insights suggesting that the SIF decreases when a multitude of micro-cracks encompass the primary crack.

Kachanov [87, 88] has shed light on the influence of micro-crack arrays and crack inclination angles on the structural geometry, resulting in either shielding effects or weakening phenomena. By exploring two distinct configurations of micro-crack distributions, namely collinear cracks and stacked cracks, He observed contrasting behaviors. Collinear cracks were associated with a stress amplification effect, leading to an increase in the SIF. In contrast, stacked configurations exhibited a stress shielding effect, causing a reduction in the SIF. He studied how crack dimensions and distances affect amplification and shielding effects. Depending on the crack distribution, these effects may compete. For mode I traction BC, he noted that when distances between collinear and stacked cracks exceed the crack length, the shielding effect dominates. For an amplification effect, Kachanov recommends smaller distances between collinear cracks compared to stacked cracks [88]. The number and orientation of cracks also impact the SIF, with more parallel stack cracks leading to a decrease in SIF. In contrast, in the scenario of a coplanar row of cracks, the SIF escalates and nears a value of 1 for the ratio of critical loads (K^*/K_0). Furthermore, the arrangement of micro-cracks surrounding the primary crack induces a stress-shielding effect. This observation has been supported by other researchers [89, 90], who have noted that arrays of micro-cracks can lead to SIF amplification at the macro-crack tip. Rotating the micro-cracks within the range of 0° to 90° (where 90° ≥ α > 0) has a notable effect on the macro-crack. The arrangement of these rotated micro-cracks leads to an escalation in the SIF as the rotation angle increases from 0° to 90°.
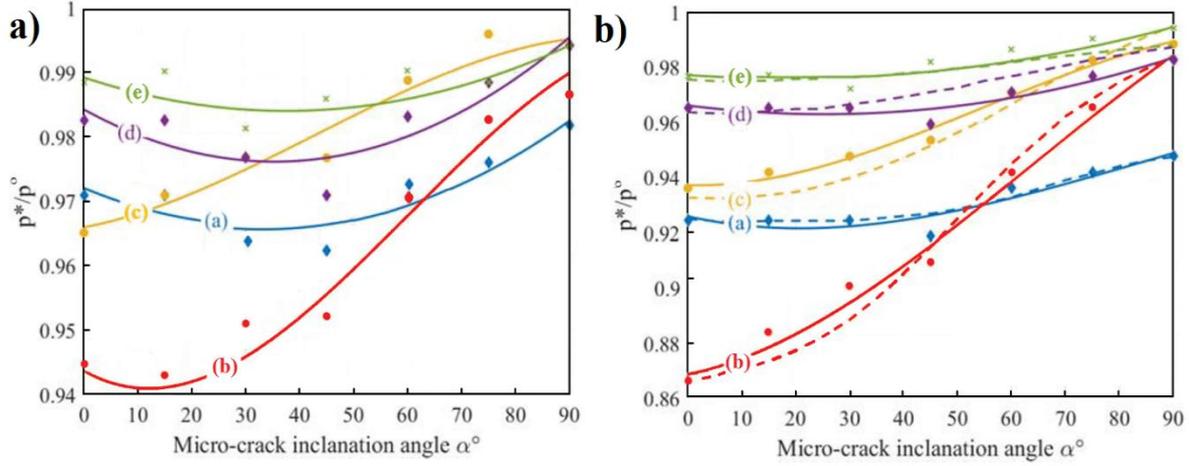
Fig. 21. The critical load ratios for various micro-crack orientations a) Constant critical stretch for micro-crack distribution (points: PD scatter data, solid lines: PD polynomial) b) Micro-crack distribution cases: K^*/K_0 = (a) 0.92, (b) 0.86, (c) 0.94, (d) 0.98, (e) 0.99 (Markers: PD scatter data, dashed lines: PD polynomials, solid lines: analytical solution for the same cases)

In the PD analysis, micro-crack distribution diagrams show that the spacing between micro-cracks is greater than the crack length ($a/s \gg a_c$), indicating a prevalent shielding effect. Consequently, SIF in setups with micro-cracks is expected to be lower than in those with a single macro-crack, resulting in $K^* < K_0$. In the PD model, the effect of micro-cracks at a rotational angle α of 0º on the SIF of the macro-crack tip is considered using analytical solutions from reference [88]. The designated relationships for K^*/K_0 in the PD model are (a) 0.92, (b) 0.86, (c) 0.94, (d) 0.98, and (e) 0.99.

The numerical model's s_c^* values are adjusted by incorporating the selected K^*/K_0 ratios to keep the calculated values below the original s_c values. Additionally, to address the impact of micro-crack orientations on the macro-crack tip, the critical stretch ratios are incrementally elevated. When the rotation angle α is 90º, the resulting values are approximately 0.0034 for cases (a)-(c) and 0.0036 for cases (d)-(e). The variation in critical shrink values among these cases stems from the positioning of the micro-cracks. Specifically, when the micro-cracks are located behind and above the macro-

crack tip at a rotation angle of 90º, the K^*/K_0 ratio drops below 0.96 [88]. Integrating the K^*/K_0 relationship into the PD model yields more accurate results compared to the analytical solution [34]. This observation provides additional confirmation of the significant role played by crack propagation with respect to both the distribution of micro-cracks and the deviation angle. It underscores the intricate relationship between these factors in influencing the structural integrity and behavior of the material under consideration.

4.6. Micro-crack Influence on Fracture Propagation in Dental Plates

To determine the crack propagation velocities, dynamic boundary conditions are applied to the dental plate illustrated in Figure 22. The plate undergoes symmetric loading with velocity constraints of $v^{**} = 0.4$ m/s enforced on the plate edges at $y = W/2$ and $y = -W/2$. The boundary conditions detailed are implemented on the fictitious boundary layer R_f, matching the horizon size ($\delta = 3.015 \, \Delta x$). These boundary conditions are enforced in accordance with equations 31-34 [91]:

$$u_f\left(x_f, y_f, t+\Delta t\right) = u\left(x, y, t\right) \quad y_f \in R_{f\left(y=\frac{w}{2}\right)} \tag{31}$$

$$v_f\left(x_f, y_f, t+\Delta t\right) = 2\overset{*}{v}\left(x, y=\frac{W}{2}, t+\Delta t\right) \times t - v(x, y, t) \tag{32}$$

$$u_f\left(x_f, y_f, t+\Delta t\right) = u\left(x, y, t\right) \quad y_f \in R_{f\left(y=\frac{w}{2}\right)} \tag{33}$$

$$v_f\left(x_f, y_f, t+\Delta t\right) = 2\overset{*}{v}\left(x, y=-\frac{W}{2}, t+\Delta t\right) \times t - v(x, y, t) \tag{34}$$
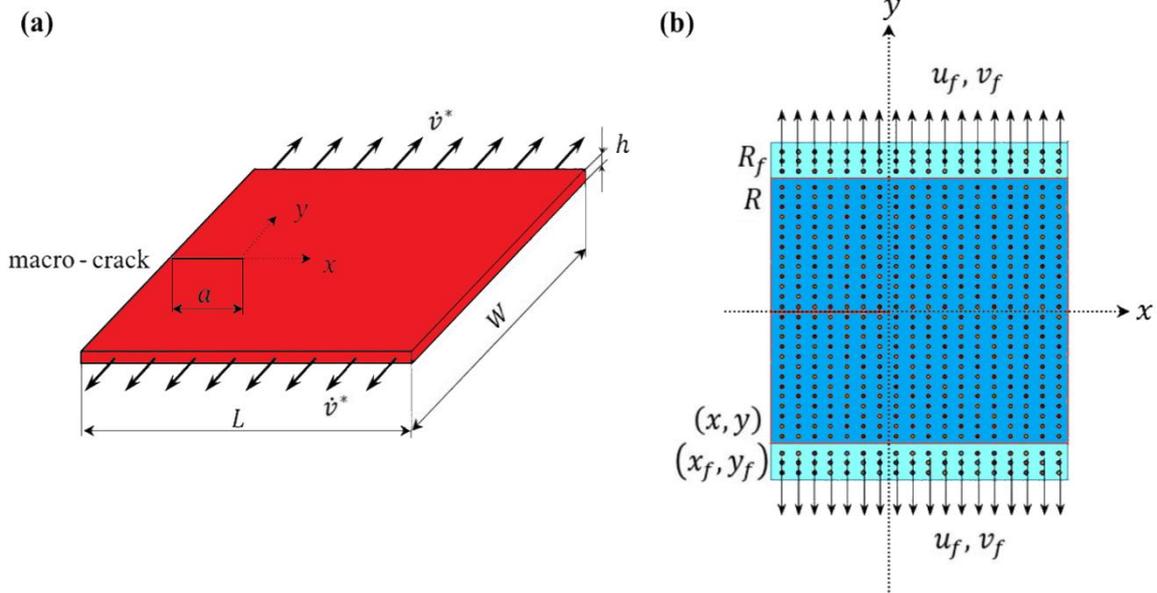
25

Fig. 22. a) Depiction of a square dental plate with a macro-crack under velocity boundary conditions. b) Discrete spatial representation of the square dental plate featuring a side macro-crack under prescribed boundary conditions, following the model by Karpenko *et* al. [26]

The PD model in Figure 22-b is discretized into 272,800 material points with a uniform spacing of $\Delta x = 6 \times 10^{-9}$ m. Simulations run with a time step of $\Delta t = 0.2$ μs and end at $t = 400$ μs. A constant fracture energy model is used, where the critical fracture energy remains consistent regardless of crack propagation speed [92]. The PD numerical models for scenarios (a) to (e) depicted in Figure 20 are first investigated by analyzing how the SIF of the macro-crack case, K_0, relates to the cases with micro-cracks, K^*. This study is conducted under consistent critical stretch conditions. Subsequently, the PD model delves into the correlation between K^*/K_0, where K^* denotes the SIF of cases featuring micro-cracks, and K_0 represents the SIF of the macro-crack case. The values of K^*/K_0 vary for each case as follows: K^*/K_0 = (a) 0.92, (b) 0.86, (c) 0.94, (d) 0.98, and (e) 0.99. The critical stretch values are adjusted by multiplying them with the corresponding K^*/K_0 ratios to implement these relationships.

In Figure 23, the damage plots for all cases are displayed under a fixed critical stretch condition. Figure 24 presents plots for cases with $K^*/K_0 \neq 1$ and varying micro-crack inclination angles (α = 0°, 45°, and 90°). Interestingly, the orientation of the micro-cracks, represented by the inclination angles, influences the macro-crack propagation behavior, showing a tendency for the macro-cracks to follow the orientation of the micro-cracks. Moreover, placing the micro-crack at the leading edge perpendicular to the macro-crack (α = 90°) results in the bifurcation of the macro-crack. The crack propagation patterns observed in both critical stretch value setups are notably similar. The PD simulation outcomes highlight the significant impact of the micro-crack types, their sizes, spatial arrangements, and orientations on the toughening mechanisms operating within the system.

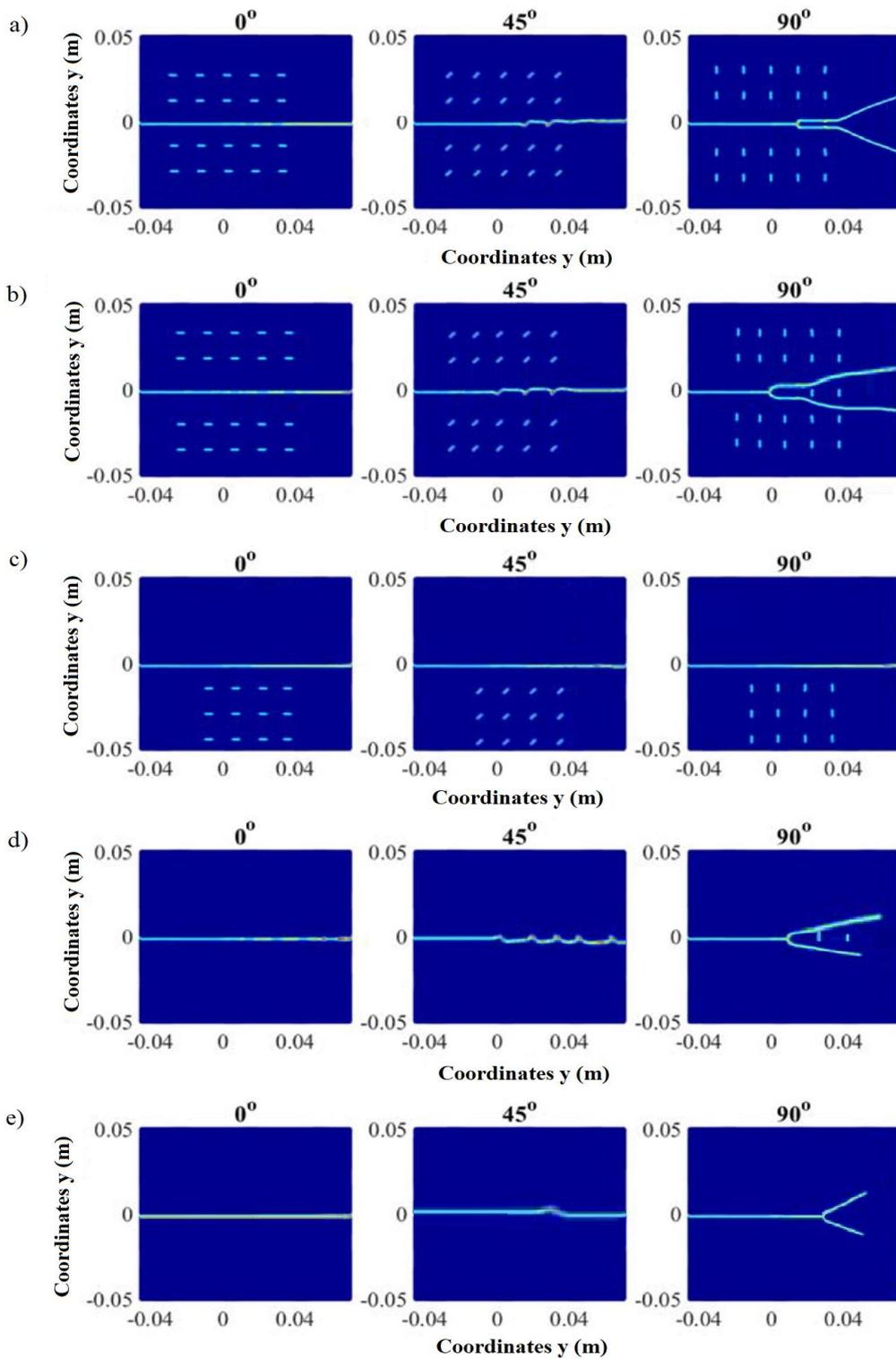**Fig. 23.** Evolution of damage resulting from crack propagation in the 3Y-TZP+ 0.025 wt% Al_2O_3 sample, with a consistent critical stretch across scenarios a to e, showcasing multiple micro-cracks oriented at angles of α = 0°, 45°, and 90°
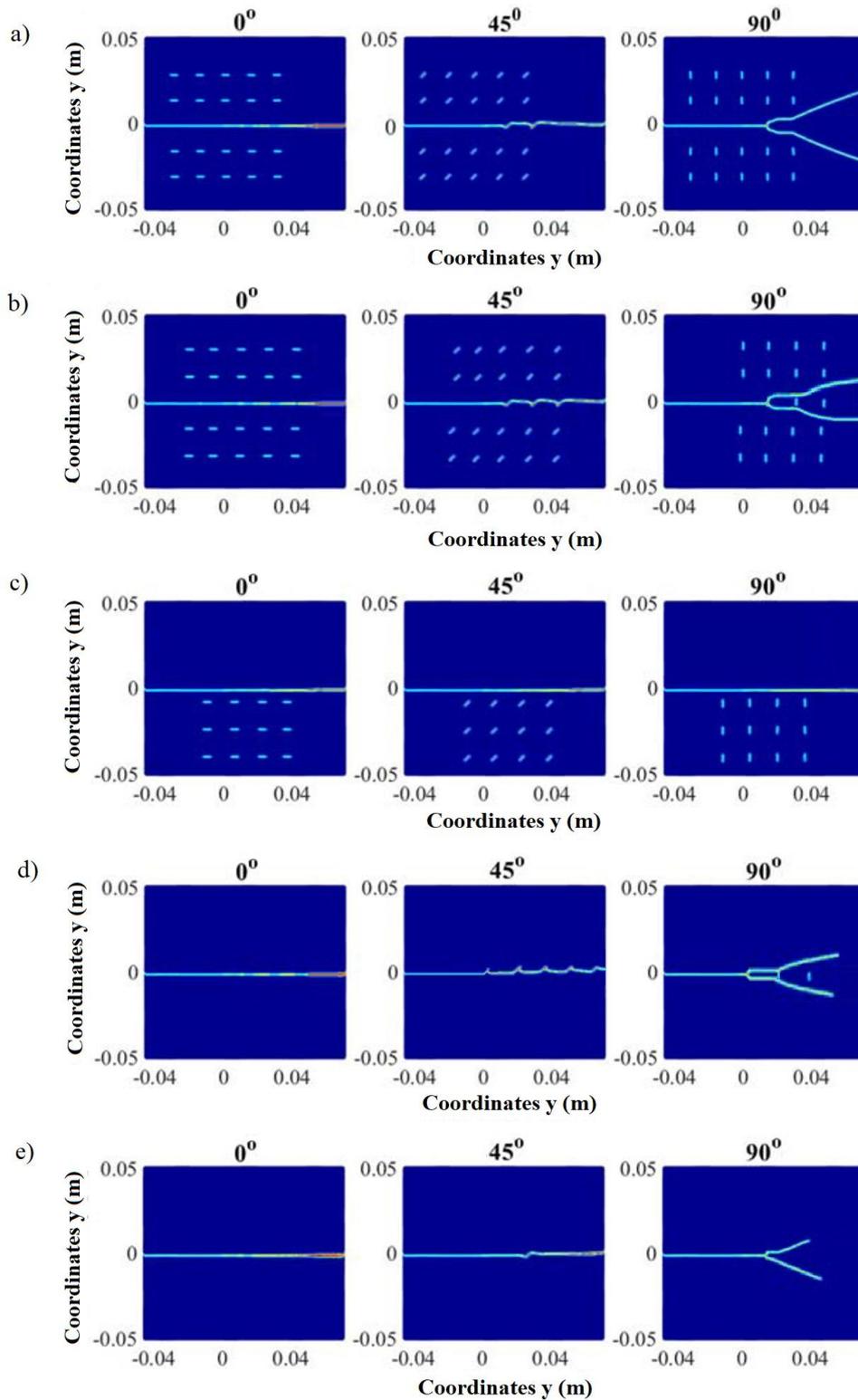
Fig. 24. Progression of damage from cases a to e, where K^*/K_0 represents the micro-crack distribution: K^*/K_0 = a) 0.92, b) 0.86, c) 0.94, d) 0.98, e) 0.99, with micro-cracks oriented at angles of α = 0°, 45°, and 90° during crack propagation in the 3Y-TZP+ 0.025 wt% Al$_2$O$_3$ sample

5. Conclusions

In the current study, a series of experiments were conducted to fabricate dental plate ceramics using a combination of 3Y-TZP + x wt% Al$_2$O$_3$. The research delved into exploring various aspects such as mechanical properties, resilience to aging, and the application of ordinary state-based peridynamics models to address complex issues associated with nanoporosities and

interactions between micro and macro-cracks. Summary of the major discoveries and insights derived from this study:

1) The specimens displayed a uniform microstructure with increased density and a grain size falling within the range of 80 nm to around 100 nm, attributed to the low-level doping of Al_2O_3.

2) By increasing the amount of Al_2O_3 additive up to 0.05 wt% in 3Y-TZP dental ceramics, the values of relative density, hardness, Young's modulus, fracture toughness, and flexural strength increased to 99.5%, 15.1 GPa, 280 GPa, 9.97 MPa.m$^{1/2}$, and 355 MPa, respectively.

3) The dental ceramics exhibited high hardness and significant fracture toughness, primarily attributed to the mechanism of phase transformation toughening.

4) Enhanced resistance to aging and superior mechanical properties were attained through the incorporation of 0.25 wt% Al_2O_3 doping.

5) Nanoporosities were found to play a critical role in structural behavior and crack propagation, as evidenced by the PD numerical model showcasing crack arrest phenomena and deviations in trajectory towards the porosities.

6) The parameter K^*/K_0 significantly impacted results, with close agreement between updated K^*/K_0 values and analytical solutions for different micro-crack distributions, indicating facilitation of crack propagation with micro-crack allocation.

7) Analysis of crack propagation speeds revealed a shielding effect with microcracks ahead of the macro-crack, reducing crack speeds by 15%.

Nomenclature

ΔV_Δ	The volume of the boundary layer
α	notched depth
θ	Dilatation between material points in PD
ρ	Density
δ	Horizon size in PD
κ	Bulk modulus in PD
μ	Shear modulus in PD
ν	Poission's ratio
2-D	2-dimensional
3-D	3-dimensional
Al_2O_3	Alumina
a/s	Micro-cracks distance
B	Width of the specimen bar
BC	Boundary condition
b	Prescribed body force density field in PD
c-ZrO_2	Cubic Zirconia
CaO	Calcium oxide
CeO_2	Ceric oxide
dp/dh	Material stiffness
E	Young's modulus
Er_2O_3	Erbium oxide
FEM	Finite element method
FESEM	Field emission scanning electron microscopy
G_c	Critical energy release rate
f_m	Volume monoclinic fraction
H	A neighborhood of x
h	Thickness parameter in PD
$H_{x(i)}$	Interaction between material point i and j within its horizon
H_v	Vickers hardness
K^*/K_0	The ratio of the critical
K_{IC}	Fracture toughness in mode I
LTD	Low-temperature degradation
l	Support span
MAJ	Mehl-Avrami-Johnson equation
MgO	Magnesium oxide
MOR	Flexural strength
m-ZrO_2	Monoclinic zirconia
P_{max}	Applied load at fracture
p	Critical load
p^*	Critical load with a macro-crack and micro-cracks
PD	Peridynamics
PSZ	Partially stabilized zirconia
SELNB	Single-edge laser-notch beam
SIF	Stress Intensity Factor
S_c	Critical stretch
s	Distance between material in PD
TPB	Three-point bending
t	A pairwise force function
t_p	Current crack tip position
t_{p-1}	Previous crack tip position
t-ZrO_2	Tetragonal zirconia
u	Displacement vector field
$\ddot{u}_{(i)}$	The acceleration of material point i at time t
V	Velocity
V_m	Volume monoclinic phase
V_{ms}	Saturation of monoclinic phase
W	The thickness of the specimen bar
XRD	X-Ray diffraction
XFEM	Extended finite element method
X_m	Proportion of the monoclinic phase relative
Y_2O_3	Yttria
YSZ	Yttria-stabilized zirconia
y	Updated position of a material point in PD
Y^*	Stress intensity shape factor
ZrO_2	Zirconia

Acknowledgments

Conflicts of Interest

The author declares that there is no conflict of interest regarding the publication of this article.

References

[1] Yanga, Y., Hua, C., Liub, Q. and Lia, J., 2024. Research progress and prospects of colored zirconia ceramics: A review. *Journal of Advanced Ceramics*, 13(10) pp. 1505-1522.

[2] Gulati, S., Kumar, S. and Baul, A., 2024. Nanoceramics: novel and benign materials in prosthodontics. In *Industrial Applications of Nanoceramics,* (pp. 79-98), Elsevier.

[3] Wang, H., Shen, F., Li, Z., Zhou, B., Zhao, P., Wang, W., Cheng, B., Yang, J., Li, B. and Wang, X., 2023. Preparation of high-performance ZrO_2 bio-ceramics by stereolithography for dental restorations. *Ceramics International*, part A, 49 (17) pp. 28048-28061.

[4] Liang, Z., Liu, X., Zhao, Z., Lu, H., Wang, H., Liu, C., Wang, M. and Song, X., 2023. Enhancing hardness and toughness of WC simultaneously by dispersed ZrO_2. *Materials Science and Engineering: A*, *870*, p. 144905.

[5] Gionea, A., Andronescu, E., Voicu, G., Bleotu, C. and Surdu, V.A., 2016. Influence of hot isostatic pressing on ZrO_2–CaO dental ceramics properties. *International Journal of Pharmaceutics*, *510*(2), pp. 439-448.

[6] Chen, H., Huang, Z.Y. and Chen, W., 2023. The fabrication and in vitro bioactivity of HA/ZrO_2/MgO gradient composite coatings. *Ceramics International*, 50(1), pp. 1814-1825.

[7] Ali, A.A., Shama, S.A., Amin, A.S. and EL-Sayed, S.R., 2021. Synthesis and characterization of ZrO_2/CeO_2 nanocomposites for efficient removal of Acid Green 1 dye from aqueous solution. *Materials Science and Engineering: B*, *269*, p. 115167.

[8] Wang, S. and Liu, J., 2021. Microstructure and growth characteristics of Al_2O_3/Er_2O_3/ZrO_2 solidified ceramics with different compositions. *Journal of the European Ceramic Society*, *41*(7), pp. 4284-4293.

[9] Zhai, S., Pan, W. and Liu, J., 2023. Regulation of Y_2O_3 addition on structure and properties of Al_2O_3/ZrO_2 (Y_2O_3) directionally solidified eutectic ceramic. *Ceramics International*, *49*(18), pp. 30240-30247.

[10] Pian, X., Fan, B., Chen, H., Zhao, B., Zhang, X. and Zhang, R., 2014. Preparation of m-ZrO_2 compacts by microwave sintering. *Ceramics International*, *40*(7), pp. 10483-10488.

[11] Dimitriadis, K., Moschovas, D., Tulyaganov, D.U. and Agathopoulos, S., 2023. Microstructure, physical and mechanical properties of dental polychromic multilayer zirconia of uniform composition. *European Journal of Oral Sciences*, p.e12959.

[12] Al-Dwairi, Z.N., Al-Aghbari, L., Husain, N.A.H. and Özcan, M., 2023. Durability of cantilever inlay-retained fixed dental prosthesis fabricated from multilayered zirconia ceramics with different designs. *Journal of the mechanical behavior of biomedical materials*, *137*, p. 105547.

[13] Zhang, F., Vanmeensel, K., Batuk M., Hadermann J., Inokoshi M., et al., 2015. Highlytranslucent, strong and aging-resistant 3Y-TZP ceramics for dental restoration by grain boundary segregation, *Acta Biomaterialia,* 16, pp.215–222.

[14] Samodurova A., Kocjan, A., Swain, M.V., Kosmac T. 2015, The combined effect of alumina and silica co-doping on the ageing resistance of 3Y-TZP bioceramics, *Acta Biomaterialia,* Biomater. 11 pp. 477–487.

[15] Seesala, V.S., Rajasekaran, R., Vaidya, P.V. and Dhara, S., 2022. Functional gradient coating of alumina on net shaped zirconia implant: Improved strength, aging resistance, and role of residual stress. *Journal of the European Ceramic Society,* 42(13), pp. 5932-5942.

[16] Salma, U., 2019. Microstructure development for optimum fracture toughness of YSZ added Al_2O_3 composites.

[17] Ross, I.M., Rainforth, W.M., Scott A.J., Brydson R., 2001, The role of trace additions of alumina to yttria–tetragonal zirconia polycrystals (Y-TZP), *Scripta Materialia*. 45, pp. 653–660.

[18] Piascik, J.R., Zhang, Q., Bower, C.A., Thompson, J.Y., Stoner, B.R., 2007. Evidence of stress-induced tetragonal-to-monoclinic phase transformation during sputter deposition of yttria-stabilized zirconia. *Journal of Materials Research,* 22(4), pp. 1105-1111.

[19] Devi, S., Chaudhary, S., Hashim, M., Batoo, K.M., Hadi, M. and Shirsath, S.E., 2024. Co-relation between Rietveld analysis, dielectric studies and impedance spectroscopy of the $Ba_{1-x}Sr_xTiO_3$ ceramics. *Journal of Materials Science: Materials in Electronics*, *35*(16), pp. 1-24.

[20] Feng, Y., Wu, D., Stewart, M.G. and Gao, W., 2023. Past, current and future trends and challenges in non-deterministic fracture mechanics: A review. *Computer Methods in Applied Mechanics and Engineering,* 412, p.116102.

[21] Li, P., Li, W., Li, B., Yang, S., Shen, Y., Wang, Q. and Zhou, K., 2023. A review on phase field models for fracture and fatigue. *Engineering Fracture Mechanics*, p. 109419.

[22] Almarghani, L.K., Shetawey, R.A. and Alassar, R.M., 2024. Marginal Accuracy and Fracture Resistance of Occlusal Veneers Constructed from Different Pressable Ceramics. *Al-Azhar Journal of Dentistry*, 11(2), p. 14.

[23] Lien, W., Minju, D.Y., Jones, S.D., Wentworth, C.V., Savett, D.A., Mansell, M.R. and Vandewalle, K.S., 2021. The effect of micro-mechanical signatures of constituent phases in modern dental restorative materials on their macro-mechanical property: A statistical nanoindentation approach. *Journal of the Mechanical Behavior of Biomedical Materials,* 120, p. 104591.

[24] He, Q., Qin, Y., Zhan, X., Zhang, W. and Ye, J., 2023. Physicochemical and biological properties of Y-TZP ceramics modified by infiltration with different bioactive glasses for dental implant. *Ceramics International,* 49(17), pp. 29187-291897.

[25] Zhang, R., Zhao, C., Xing, J., Niu, J., Chen, H. and Qian, Y., 2023. Macro and micro investigation of fracture behavior and crack evolution considering inherent microcrack in prefabricated flawed granite. *Engineering Fracture Mechanics,* 284, p. 109264.

[26] Karpenko, O., Oterkus, S. and Oterkus, E., 2020. Influence of different types of small-size defects on propagation of macro-cracks in brittle materials. *Journal of Peridynamics and Nonlocal Modeling,* 2, pp. 289-316.

[27] Candaş, A., Oterkus, E. and İmrak, C.E., 2021. Dynamic crack propagation and its interaction with micro-cracks in an impact problem. *Journal of Engineering Materials and Technology,* 143(1), p. 011003.

[28] Teng, Z.H., Liao, D.M., Wu, S.C., Sun, F., Chen, T. and Zhang, Z.B., 2019. An adaptively refined XFEM for the dynamic fracture problems with micro-defects. *Theoretical and Applied Fracture Mechanics*, *103*, p.102255.

[29] Chen, R., Li, B. and Xu, K., 2022. Effect of particle morphology on fatigue crack propagation mechanism of TiB_2-reinforced steel matrix composites. *Engineering Fracture Mechanics*, *274*, p.108752.

[30] Moussa, W.A., 2000. *Finite element study of the interaction and shielding effects of multiple cracks in three-dimensions* (Doctoral dissertation, Carleton University).

[31] Bouiadjra, B.B., Benguediab, M., Elmeguenni, M., Belhouari, M., Serier, B. and Aziz, M.N.A., 2008. Analysis of the effect of micro-crack on the plastic strain ahead of main crack in aluminium alloy 2024 T3. *Computational materials science*, *42*(1), pp. 100-106.

[32] Chudnovsky, A. and Wu, S., 1991. Elastic interaction of a crack with a random array of microcracks. *International Journal of Fracture*, *49*, pp. 123-140.

[33] Rose, L.R.F., 1986. Microcrack interaction with a main crack. *International journal of fracture*, *31*, pp.233-242.

[34] Petrova, V., Tamuzs, V. and Romalis, N., 2000. A survey of macro-microcrack interaction problems.

[35] Li, J., Yang, B., Wang, S., James, M.N., Xiao, S., Zhu, T. and Yang, G., 2023. Modified Model of Crack Tip Stress Field Considering Dislocation Slip Accumulation and Crack Tip Blunting. *Chinese Journal of Mechanical Engineering*, *36*(1), pp. 1-14.

[36] Wang, F. and Wang, M., 2020. Effect of holes on dynamic crack propagation under impact loading. *Applied Sciences*, *10*(3), p. 1122.

[37] Demirel, M.G., Mohammadi, R. and Keçeci, M., 2023. Crack Propagation and Fatigue Performance of Partial Posterior Indirect Restorations: An Extended Finite Element Method Study. *Journal of Functional Biomaterials*, *14*(9), p. 484.

[38] Milios, J. and Spathis, G., 1988. Dynamic interaction of a propagating crack with a hole boundary. *Acta mechanica*, *72*(3-4), pp. 283-295.

[39] Theocaris, P.S. and Milios, J., 1981. Crack arrest modes of a transverse crack going through a longitudinal crack or a hole.

[40] Yi, W., Rao, Q.H., Luo, S., Shen, Q.Q. and Li, Z., 2020. A new integral equation method for calculating interacting stress intensity factor of multiple crack-hole problem. *Theoretical and Applied Fracture Mechanics*, *107*, p. 102535.

[41] Ganesh, K.V., Islam, M.R.I., Patra, P.K. and Travis, K.P., 2022. A pseudo-spring based SPH framework for studying fatigue crack propagation. *International Journal of Fatigue*, *162*, p. 106986.

[42] Belytschko, T., Liu, W.K., Moran, B. and Elkhodary, K., 2014. *Nonlinear finite elements for continua and structures*. John wiley & sons.

[43] Wang, H., Liu, Z., Xu, D., Zeng, Q. and Zhuang, Z., 2016. Extended finite element method analysis for shielding and amplification effect of a main crack interacted with a group of nearby parallel microcracks. *International Journal of Damage Mechanics*, *25*(1), pp. 4-25.

[44] Dorduncu, M., Ren, H., Zhuang, X., Silling, S., Madenci, E. and Rabczuk, T., 2024. A review of peridynamic theory and nonlocal operators along with their computer implementations. *Computers & Structures,* 299, p. 107395.

[45] Silling, S.A., Weckner, O., Askari, E. and Bobaru, F., 2010. Crack nucleation in a peridynamic solid. *International Journal of Fracture*, *162*, pp. 219-227.

[46] Huang, D., Lu, G. and Qiao, P., 2015. An improved peridynamic approach for quasi-static elastic deformation and brittle fracture analysis. *International Journal of Mechanical Sciences*, *94*, pp. 111-122.

[47] Ha, Y.D. and Bobaru, F., 2011. Characteristics of dynamic brittle fracture captured with peridynamics. *Engineering Fracture Mechanics*, *78*(6), pp. 1156-1168.

[48] Bobaru, F. and Hu, W., 2012. The meaning, selection, and use of the peridynamic horizon and its relation to crack branching in brittle materials. *International journal of fracture*, *176*, pp. 215-222.

[49] Basoglu, M.F., Zerin, Z., Kefal, A. and Oterkus, E., 2019. A computational model of peridynamic theory for deflecting behavior of crack propagation with micro-cracks. *Computational Materials Science*, *162*, pp. 33-46.

[50] Vazic, B., Wang, H., Diyaroglu, C., Oterkus, S. and Oterkus, E., 2017. Dynamic propagation of a macrocrack interacting with parallel small cracks. *AIMS Materials Science*, *4*(1), pp. 118-136.

[51] Yoffe, E.H., 1951. LXXV. The moving griffith crack. *The London, Edinburgh, and Dublin Philosophical Magazine and Journal of Science*, *42*(330), pp. 739-750.

[52] Silling, S.A., Epton, M., Weckner, O., Xu, J. and Askari, E., 2007. Peridynamic states and constitutive modeling. *Journal of elasticity*, *88*, pp. 151-184.

[53] Silling, S.A. and Askari, E., 2005. A meshfree method based on the peridynamic model of solid mechanics. *Computers & structures*, *83*(17-18), pp. 1526-1535.

[54] Kilic, B. and Madenci, E., 2010. An adaptive dynamic relaxation method for quasi-static simulations using the peridynamic theory. *Theoretical and Applied Fracture Mechanics*, *53*(3), pp. 194-204.

[55] Madenci, E. and Oterkus, E., 2013. Peridynamic theory. In *Peridynamic theory and its applications* (pp. 19-43). New York, NY: Springer New York.

[56] Silling, S.A. and Bobaru, F., 2005. Peridynamic modeling of membranes and fibers. *International Journal of Non-Linear Mechanics*, *40*(2-3), pp. 395-409.

[57] ASTM-C373. 1999. Standard Test Method for Water Absorption, Bulk Density, Apparent, Porosity, and Apparent Specific Gravity of Fired Whiteware Products. American Standard and Testing Materials. C373-88 (ASTM).

[58] Moradkhani, A. and Baharvandi, H., 2018. Effects of additive amount, testing method, fabrication process and sintering temperature on the mechanical properties of Al_2O_3/3Y-TZP composites. *Engineering Fracture Mechanics,* 191, pp. 446-460.

[59] Zhang, W., Bao, J., Xu, J., Wu, X., Li, D., Song, X. and An, S., 2017. Composition dependence of the adjustable microstructure and mechanical properties of ytterbia-ceria-costabilised TZP. *Journal of Alloys and Compounds,* 727, pp. 627-632.

[60] Toraya, H., Yoshimura, M. and Somiya, S., 1984. Calibration curve for quantitative analysis of the monoclinic-tetragonal ZrO_2 system by X-ray diffraction. *Journal of the American Ceramic Society,* 67(6), pp. C-119.

[61] Garvie, R.C. and Nicholson, P.S., 1972. Phase analysis in zirconia systems. *Journal of the American Ceramic Society,* 55(6), pp. 303-305.

[62] Chevalier, J., Cales, B. and Drouin, J.M., 1999. Low-temperature aging of Y-TZP ceramics. *Journal of the American Ceramic Society*, 82(8), pp.2150-2154.

[63] Kohorst, P., Borchers, L., Strempel, J., Stiesch, M., Hassel, T., Bach, F.W. and Hübsch, C., 2012. Low-temperature degradation of different zirconia ceramics

for dental applications. *Acta biomaterialia,* 8(3), pp. 1213-1220.

[64] Moradkhani, A., Panahizadeh, V. and Hoseinpour, M., 2023. Indentation fracture resistance of brittle materials using irregular cracks: A review. *Heliyon.*

[65] Zorzi, J.E. and Perottoni, C.A., 2013. Estimating Young's modulus and Poisson's ratio by instrumented indentation test. *Materials Science and Engineering: A*, *574*, pp. 25-30.

[66] Hardness, A.B., 1999. Standard Test Method for Microindentation Hardness of Materials. ASTM Committee: West Conshohocken, PA, USA, 384, p. 399.

[67] ASTM International. ASTM C769-98. Standard test method for sonic velocity in manufactured carbon and graphite materials for use in obtaining an approximate Young's modulus.

[68] Moradkhani, A., Baharvandi, H. and Naserifar, A., 2019. Fracture toughness of 3Y-TZP dental ceramics by using vickers indentation fracture and SELNB methods. *Journal of the Korean Ceramic Society*, *56*(1), pp. 37-48.

[69] Guinea, G.V., Pastor, J.Y., Planas, J. and Elices, M., 1998. Stress intensity factor, compliance and CMOD for a general three-point-bend beam. *International Journal of Fracture*, *89*, pp. 103-116.

[70] ASTM Committee C-1161 on Advanced Ceramics, 2013. *Standard test method for flexural strength of advanced ceramics at ambient temperature*. ASTM International.

[71] áSakib Khan, M., áSaiful Islam, M. and Bates, D., 1998. Cation doping and oxygen diffusion in zirconia: a combined atomistic simulation and molecular dynamics study. *Journal of Materials Chemistry*, *8*(10), pp. 2299-2307.

[72] Gaillard, Y., Anglada, M. and Jiménez-Piqué, E., 2009. Nanoindentation of yttria-doped zirconia: Effect of crystallographic structure on deformation mechanisms. *Journal of materials research*, *24*(3), pp. 719-727.

[73] Moradkhani, A., Baharvandi, H. and Naserifar, A., 2019. Effect of sintering temperature on the grain size and mechanical properties of Al_2O_3-SiC Nanocomposites. *Journal of the Korean Ceramic Society,* 56(3), pp. 256-268.

[74] Moradkhani, A.R., Baharvandi, H.R., Vafaeesefat, A. and Tajdari, M., 2012. Microstructure and mechanical properties of Al_2O_3-SiC nanocomposites with 0.05% MgO and different SiC volume fraction.

[75] Twigg, P.C., Riley, F.L. and Roberts, S.G., 2002. Nanoindentation investigation of micro-fracture wear mechanisms in polycrystalline alumina. *Journal of materials science,* 37, pp. 845-853.

[76] Krell, A. and Schädlich, S.J.M.S., 2001. Nanoindentation hardness of submicrometer alumina ceramics. *Materials Science and Engineering: A,* 307(1-2), pp. 172-181.

[77] Stollberg, D.W., Hampikian, J.M., Riester, L. and Carter, W.B., 2003. Nanoindentation measurements of combustion CVD Al_2O_3 and YSZ films. *Materials Science and Engineering: A*, 359(1-2), pp. 112-118.

[78] Wang, J. and Stevens, R., 1989. Zirconia-toughened alumina (ZTA) ceramics. *Journal of Materials science*, 24, pp. 3421-3440.

[79] Jing, Q., Bao, J., Ruan, F., Song, X., An, S., Zhang, Y., Tian, Z., Lv, H., Gao, J. and Xie, M., 2019. High-fracture toughness and aging-resistance of 3Y-TZP ceramics with a low Al_2O_3 content for dental applications. *Ceramics International*, *45*(5), pp. 6066-6073.

[80] Zhang, F., Chevalier, J., Olagnon, C., Van Meerbeek, B. and Vleugels, J., 2017. Slow crack growth and hydrothermal aging stability of an alumina-toughened zirconia composite made from La_2O_3-doped 2Y-TZP. *Journal of the European Ceramic Society*, *37*(4), pp. 1865-1871.

[81] Mercer, C., Williams, J.R., Clarke, D.R. and Evans, A.G., 2007. On a ferroelastic mechanism governing the toughness of metastable tetragonal-prime (t′) yttria-stabilized zirconia. *Proceedings of the Royal Society A: Mathematical, Physical and Engineering Sciences*, *463*(2081), pp. 1393-1408.

[82] Zhao, M., Ren, X. and Pan, W., 2014. Effect of lattice distortion and disordering on the mechanical properties of titania-doped yttria-stabilized zirconia. *Journal of the American Ceramic Society*, *97*(5), pp. 1566-1571.

[83] Zarone, F., Russo, S. and Sorrentino, R., 2011. From porcelain-fused-to-metal to zirconia: clinical and experimental considerations. *Dental materials*, *27*(1), pp. 83-96.

[84] Vijan, K.V., 2017. An overview of the current survival status and clinical recommendation for porcelain fused to metal vs all-ceramic Zirconia posterior fixed partial dentures. *World Journal Dentistry*, 8(2), pp. 145-50.

[85] Yang, R.S., Ding, C.X., Yang, L.Y., Xu, P. and Chen, C., 2018. Hole defects affect the dynamic fracture behavior of nearby running cracks. *Shock and Vibration*, *2018*.

[86] Chen, Z. and Chu, X., 2021. Peridynamic modeling and simulation of fracture process in fiber-reinforced concrete. *Computer Modeling in Engineering & Sciences,* 127(1), pp. 241-272.

[87] Kachanov, M., 1986. On crack-microcrack interactions. *International Journal of Fracture*, *30*, pp. R65-R72.

[88] Kachanov, M., 1993. Elastic solids with many cracks and related problems. *Advances in applied mechanics*, *30*, pp. 259-445.

[89] Gong, S.X. and Horii, H., 1989. General solution to the problem of microcracks near the tip of a main crack. *Journal of the Mechanics and Physics of Solids*, *37*(1), pp. 27-46.

[90] Romalis, N.B. and Tamuzh, V.P., 1984. Propagation of a main crack in a body with distributed microcracks. *Mechanics of Composite Materials*, *20*(1), pp. 35-43.

[91] Madenci, E. and Oterkus, S., 2016. Ordinary state-based peridynamics for plastic deformation according to von Mises yield criteria with isotropic hardening. *Journal of the Mechanics and Physics of Solids*, *86*, pp. 192-219.

[92] Chandar, K.R. and Knauss, W.G., 1982. Dynamic crack-tip stresses under stress wave loading—a comparison of theory and experiment. *International Journal of Fracture*, *20*, pp.209-222.